

# The impact of internal variability on benchmarking deep learning climate emulators

Björn Lütjens<sup>1</sup>, Raffaele Ferrari<sup>1</sup>, Duncan Watson-Parris<sup>2</sup>, Noelle Selin<sup>1,3,4</sup>

<sup>1</sup>Department of Earth, Atmospheric, and Planetary Sciences, Massachusetts Institute of Technology

<sup>2</sup>Scripps Institution of Oceanography and Halicioğlu Data Science Institute,  
University of California, San Diego

<sup>3</sup>Institute for Data, Systems and Society, Massachusetts Institute of Technology

<sup>4</sup>Center for Sustainability Science and Strategy, Massachusetts Institute of Technology

## Key Points:

- Linear regression outperforms deep learning for emulating 3 out of 4 spatial atmospheric variables in the ClimateBench benchmark
- Deep learning emulators can overfit unpredictable (multi-)decadal fluctuations, when trained on a few ensemble realizations only
- We recommend evaluating climate emulation techniques on large ensembles, such as the Em-MPI data subset with means over 50 realizations

arXiv:2408.05288v2 [cs.LG] 31 Mar 2025

**Abstract**

Full-complexity Earth system models (ESMs) are computationally very expensive, limiting their use in exploring the climate outcomes of multiple emission pathways. More efficient emulators that approximate ESMs can directly map emissions onto climate outcomes, and benchmarks are being used to evaluate their accuracy on standardized tasks and datasets. We investigate a popular benchmark in data-driven climate emulation, ClimateBench, on which deep learning-based emulators are currently achieving the best performance. We compare these deep learning emulators with a linear regression-based emulator, akin to pattern scaling, and show that it outperforms the incumbent 100M-parameter deep learning foundation model, ClimaX, on 3 out of 4 regionally-resolved climate variables, notably surface temperature and precipitation. While emulating surface temperature is expected to be predominantly linear, this result is surprising for emulating precipitation. Precipitation is a much more noisy variable, and we show that deep learning emulators can overfit to internal variability noise at low frequencies, degrading their performance in comparison to a linear emulator. We address the issue of overfitting by increasing the number of climate simulations per emission pathway (from 3 to 50) and updating the benchmark targets with the respective ensemble averages from the MPI-ESM1.2-LR model. Using the new targets, we show that linear pattern scaling continues to be more accurate on temperature, but can be outperformed by a deep learning-based technique for emulating precipitation. We publish our code and data at [github.com/blutjens/climate-emulator](https://github.com/blutjens/climate-emulator).

**Plain Language Summary**

Running a state-of-the-art climate model for a century-long future projection can take multiple weeks on the world's largest supercomputers. Emulators are approximations of climate models that quickly compute climate forecasts when running the full climate model is computationally too expensive. Our work examines how different emulation techniques can be compared with each other. We find that a simple linear regression-based emulator can forecast local temperatures and rainfall more accurately than a complex machine learning-based emulator on a commonly used benchmark dataset. It is surprising that linear regression is better for local rainfall, which is expected to be more accurately emulated by nonlinear techniques. We identify that noise from natural variations in climate, called internal variability, is one reason for the comparatively good performance of linear regression on local rainfall. This implies that addressing internal variability is necessary for assessing the performance of climate emulators. Thus, we assemble a benchmark dataset with reduced internal variability and, using it, show that a deep learning-based emulator can be more accurate for emulating local rainfall, while linear regression continues to be more accurate for temperature.

**1 Introduction**

Earth system models (ESMs) are usually run many times to fully account for humanity's imperfect knowledge of future emissions and the chaotic nature of Earth's dynamics. But many runs come at a cost: Simulating the climate effects of a single emission pathway can take weeks and require computing resources worth hundreds of thousands of USD<sup>1</sup>. As a result, full-complexity ESMs are often only run for a few representative emission pathways and more efficient "climate emulators" are used for applications in climate science, finance, or governance that require custom pathways (Matthews et al., 2021; Lütjens, 2023; Richters et al., 2024). These emulators are trained to approximate the climate projections of an ESM for

---

<sup>1</sup> For example, 325K USD in cloud compute assuming the reference MPI-ESM1.2-HR model (Müller et al., 2018) would have been run on AWS at 1.53 USD/36vCPU hrs with 100km res. and 5 realizations per 250-year pathway and 400 wall-clock hrs per realization on 106x 36-core nodes, totaling ~7.6M CPU hrs.

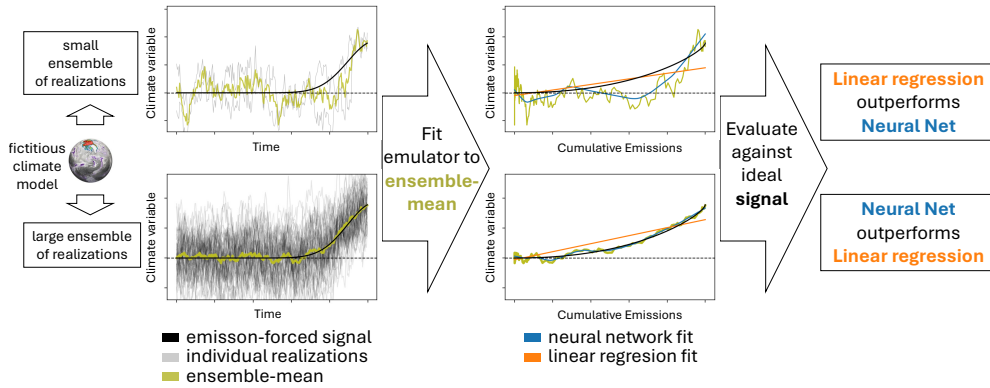


Figure 1: **A cartoon illustrating the impact of internal variability on benchmarking deep learning emulators.** The figure is generated with a mock-up stochastic model described in Section 2.6. The model is a nonlinear function that relates fictitious greenhouse gas emissions to nonlinear changes in an imagined climate variable. Each realization of this function is noisy, representing fluctuations from internal variability in the climate system that remains fundamentally unpredictable over long timescales. When training an emulator to approximate this model when it has only been run a few times for the given emission scenario, neural networks can overfit to low-frequency components of these fluctuations (top-row). A simple linear approach represents the emission-forced signal more accurately, despite the opposite being the case when many realizations are available (bottom-row). To compare emulation techniques more reliably, we recommend using large climate model ensembles that attenuate the influence of internal variability.

a given emission pathway and, recently, deep learning has been proposed as a novel technique to solve this function approximation problem. In this work, motivated by growing concerns about reproducibility and overly optimistic results in deep learning (Kapoor & Narayanan, 2023), we reevaluate this emerging technique from the perspective of established practices within the climate science community.

Existing emulation techniques can be broadly distinguished into physics-based, data-driven, or hybrid combinations, following the definition in (Matthews et al., 2021). Physics-based techniques, such as reduced-complexity climate models, solve simplified sets of differential equations and are often focused on projecting an annually- and globally-averaged climate (Meinshausen et al., 2011; C. Smith, 2021; Dorheim et al., 2023); reviewed in (Sarofim et al., 2021). In comparison, data-driven techniques often target higher spatial and temporal resolutions and are fitted to projections of the full-complexity ESMs (Tebaldi et al., 2025). For example, linear pattern scaling (LPS) takes global surface temperature,  $\bar{T}$ , as input and emulates the locally-resolved change of any atmospheric climate variable, such as surface temperature or precipitation, as a linear function of  $\bar{T}$  (Santer et al., 1990). LPS is possibly the most frequently used climate emulation technique, but is known to break down for emulating locally-resolved aerosol impacts, nonlinear precipitation events, or overshoot scenarios, among others (Tebaldi & Arblaster, 2014; Lee et al., 2021; Giani et al., 2024). Deep learning techniques may overcome these limitations, for example, by mapping regional emissions directly onto climate projections (Watson-Parris et al., 2022), downscaling physics-based emulators (Bassetti et al., 2024), or autoregressively emulating ESM dynamics (Bire et al., 2023; Watt-Meyer et al., 2023; Wang et al., 2024). With this increasing array of techniques, intercomparison projects that evaluate the advantages and disadvantages of each technique are becoming more important.

Benchmarks, such as ClimateBenchv1.0, define standardized datasets, tasks, and metrics for evaluating deep learning-based emulation techniques (Watson-Parris et al., 2022; Kaltenborn et al., 2023). However, they do not yet include a fully representative comparison with well-established techniques, such as LPS. In the ClimateBenchv1.0 benchmark (hereafter ClimateBench), emission pathways are used as inputs and climate variables, such as locally-resolved surface temperature are used as targets. Emulators including a vision transformer (Cli-ViT), a foundation model (ClimaX), a CNN-LSTM (Neural Network), a random forest model, and a Gaussian Process have been evaluated on it, as referenced in Table 1. LPS has also been evaluated on ClimateBench and performs very well (Watson-Parris et al., 2022). But, the existing LPS implementation used part of the target data (global mean temperatures) as inputs. Despite this being common practice for LPS (Beusch et al., 2020), it gave LPS an advantage over other emulators which were required to use only emission data as inputs. As a result, no fully representative comparison could be made and follow-up studies have cited deep-learning based emulators as the best performing techniques on ClimateBench (Nguyen et al., 2023; Kaltenborn et al., 2023). It remains an open question if deep learning can outperform traditional emulators.

Moreover, current climate emulation benchmarks do not sufficiently address internal variability in the climate system. Internal variability, i.e., natural fluctuations in weather or climate (Leith, 1978, and Appendix A1), can be of similar or exceeding magnitude as the emission-forced signals (Hawkins & Sutton, 2009). To identify forced signals despite the presence of internal variability, researchers often take an ensemble-mean over a sufficiently large set of climate simulations with perturbed initial conditions, i.e., realizations or ensemble members (Maher et al., 2021). Similarly, the ClimateBench target climate variables are ensemble-means over three realizations from a single model that was run for the same emission pathways and slightly different initial conditions. However, three realizations are insufficient to separate the predictable forced signal from the unpredictable internal variability depending on the variable and timescales, as discussed in Tebaldi et al. (2021) and the ClimateBench paper (Watson-Parris et al., 2022).

We compare LPS with a deep learning-based emulator and investigate the impacts of internal variability on benchmarking climate emulators. First, we implement a representative comparison with LPS on ClimateBench and demonstrate that LPS outperforms all deep learning-based emulators previously evaluated on ClimateBench in emulating regionally-resolved annual mean temperature, precipitation, and extreme precipitation (according to the ClimateBench evaluation protocol). This good performance of LPS is notable given the known nonlinear relationships in precipitation. Then, we use data from the MPI-ESM1.2-LR ensemble with 50 realizations per emission pathway (Olonscheck et al., 2023), hereafter abbreviated as *Em-MPI data*, to evaluate the effect of internal variability on benchmarking. As illustrated for an idealized problem in Fig. 1, we demonstrate that high levels of internal variability in the target data can make deep learning emulators prone to overfitting and skew the benchmarking results in favor of emulation techniques with lower model complexity, such as LPS. After reducing the internal variability by averaging over many realizations, we find that a deep learning-based emulator (CNN-LSTM) can be more accurate than LPS for spatial precipitation, while LPS continues to be the more accurate emulation technique for surface temperature. In summary, addressing internal variability is necessary to make conclusive comparisons between emulation techniques.

## 2 Data & Methods

In Section 2.1, we review the targets, inputs, evaluation protocol, and metrics that are used in ClimateBench. In Section 2.2, we describe the Em-MPI data and the associated update to the targets. In Section 2.3, we detail LPS and, in Section 2.4, our reimplementations of the CNN-LSTM from (Watson-Parris et al., 2022) with specifics in Appendix B3. In Section 2.5, we introduce our “internal variability experiment” which uses the Em-MPI targets to measure how internal variability affects the relative performance of these two

emulators. In Section 2.6, we introduce a simplified dataset to test if deep learning-based models can overfit to internal variability.

## 2.1 Background on the ClimateBench benchmark

Key components of an ML benchmark are the input and target datasets and an evaluation protocol that prescribes data splits and evaluation metrics (Dueben et al., 2022). The ClimateBench inputs and targets are derived from emission pathways and associated climate projections from three realizations of the climate model, NorESM2-LM (Seland et al., 2020), for each of seven emission scenarios,  $e \in \mathbb{S}_e = \{\text{hist-ghg}, \text{hist-aer}, \text{historical}, \text{ssp126}, \text{ssp245}, \text{ssp370}, \text{ssp585}\}$ . The “ssp” and “hist-” scenarios are Shared Socioeconomic Pathway- (ssp) and single-forcer-experiments in the ScenarioMIP and DAMIP activities within the Coupled Model Intercomparison Project Phase 6 (CMIP6) (O’Neill et al., 2016; Gillett et al., 2016; Eyring et al., 2016). The data for each historical scenario encapsulates  $T_{\text{hist}} = 165$  (1850-2014) years and  $T_{\text{ssp}} = 86$  (2015-2100) years for each ssp, and, each realization is distinguished by a different initial condition.

The ClimateBench targets are locally-resolved annually-averaged climate variables, as projected by the climate model. These target variables are surface temperature (tas), diurnal temperature range (dtr), precipitation (pr), and 90th percentile precipitation (pr90). All variables are ensemble-mean anomalies, i.e., during preprocessing the projections were averaged over three realizations per emission scenario and long-term averages of a 500-year (1350-1850) preindustrial control run were subtracted from it. The dimensionality of the target dataset of each variable is  $I \times J \times \sum_{e \in \mathbb{S}_e} T_e$  with  $I = 96$  and  $J = 144$  latitudinal and longitudinal grid points corresponding to a  $(1.875^\circ \times 2.5^\circ)$  model resolution and  $T_e = \{T_{\text{hist}}$  if  $e$  starts with *hist*;  $T_{\text{ssp}}$  if  $e$  starts with *ssp* $\}$  simulated years.

The ClimateBench input dataset contains four variables for each emission scenario: globally-averaged cumulative emissions of carbon dioxide ( $\text{CO}_2^{\text{cum}}$ ), globally-averaged emissions of methane ( $\text{CH}_4$ ), and spatial maps of emissions of sulfur dioxide ( $\text{SO}_2$ ) and black carbon (BC). For each year, BC and  $\text{SO}_2$  are locally-resolved ( $I \times J$ ) matrices and  $\text{CO}_2^{\text{cum}}$  and  $\text{CH}_4$  are globally-aggregated scalars. The variables are detailed in Appendix B11.

The ClimateBench evaluation protocol prescribes the following data splits and evaluation metrics. All scenarios except for one are used as the training set, i.e.,  $\mathbb{S}_{e,\text{train}} = \{\text{hist-ghg}, \text{hist-aer}, \text{historical}, \text{ssp126}, \text{ssp370}, \text{ssp585}\}$ , resulting in  $\sum_{e \in \mathbb{S}_{e,\text{train}}} T_e = 753$  training years that are used by an optimizer to find the best model weights or parameters. The ClimateBench protocol does not prescribe a separate validation set, meaning that emulation techniques may hold out any samples from the training set and use them as validation set for choosing hyperparameters. The years 2080-2100 in ssp245 are used as the evaluation or test set, which is recommended to be unseen until reporting the scores in the results table (Goodfellow et al., 2016). The years 2015-2079 in ssp245 are not used due to their similarity to training and test scenarios.

The evaluation metrics in the ClimateBench results table in Table 1 are “spatial”, “global”, and “total” normalized root mean square errors (NRMSEs) between the predicted,  $\hat{\mathbf{Y}}_e$ , and ensemble-mean target climate variable,  $\mathbb{E}_{\mathbb{M}}[\mathbf{Y}_e]$ . We provide equations for the normalization coefficient and “total” NRMSE in Appendix B12. The spatial and global scores,  $\text{RMSE}_s$  and  $\text{RMSE}_g$ , which are used in the ClimateBench NRMSE and our experiments are calculated as follows:

$$\text{RMSE}_s(\hat{\mathbf{Y}}_e, \mathbb{E}_{\mathbb{M}}[\mathbf{Y}_e]) = \frac{1}{\sum_i \alpha_i J} \sum_{i,j} \alpha_i \sqrt{\left( \frac{1}{|\mathbb{T}_{\text{test}}|} \sum_t \hat{y}_{i,j,t,e} - \frac{1}{|\mathbb{T}_{\text{test}}|} \sum_t y_{i,j,t,e} \right)^2} \quad (1)$$

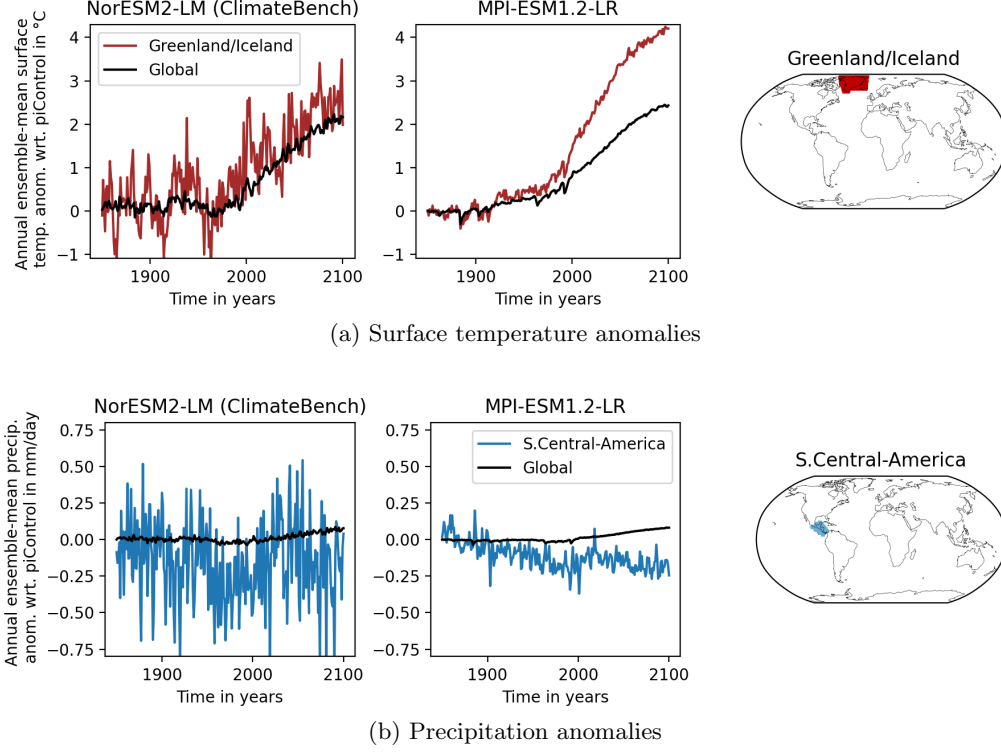


**Figure 2: Internal variability in 3-member NorESM2-LM vs. 50-member MPI-ESM1.2-LR ensemble-mean.** The plots show the ensemble-mean of the global (black) and regionally-averaged surface temperature (top-red) and precipitation (bottom-blue) anomalies from the *historical* and *ssp245* scenario. The left plots show the NorESM data that is used in the ClimateBench test set and the middle plots show the Em-MPI data. The regional averages are calculated over displayed IPCC AR6 reference regions (right). The interannual fluctuations from internal variability are visibly smaller in the 50-member Em-MPI data in comparison to the 3-member NorESM data, especially at the regional scale. More regions are shown in Fig. C4.

$$\text{RMSE}_g(\hat{\mathbf{Y}}_e, \mathbb{E}_{\mathbb{M}}[\mathbf{Y}_e]) = \frac{1}{|\mathbb{T}_{\text{test}}|} \sum_t \sqrt{\left( \frac{1}{\sum_i \alpha_i J} \sum_{i,j} \alpha_i \hat{y}_{i,j,t,e} - \frac{1}{\sum_i \alpha_i J} \sum_{i,j} \alpha_i y_{i,j,t,e} \right)^2} \quad (2)$$

where the  $i, j, t, m, e$  indices refer to latitude, longitude, year, realization ID, and emission scenario, respectively. First, the ensemble-mean over all realizations is computed,  $\mathbb{E}_{\mathbb{M}}[\mathbf{Y}_e] = \frac{1}{|\mathbb{M}|} \sum_m \mathbf{Y}_{m,e}$  with  $y_{i,j,t,e} = \frac{1}{|\mathbb{M}|} \sum_m y_{i,j,t,m,e}$ . Then, the spatial RMSE computes the per-pixel error of 21-year averages (2080-2100). The global RMSE computes the per-year error of global averages. Global averages are taken with latitude weights,  $\alpha_i = \cos(\phi_i)$ , where  $\phi_i \in [-\frac{\pi}{2}, \frac{\pi}{2}]$ . The indices are in the sets  $i \in \mathbb{I} = \{1, 2, \dots, I\}$ ,  $j \in \mathbb{J} = \{1, 2, \dots, J\}$ ,  $t \in \mathbb{T}_{\text{test}} = \{2080, 2081, \dots, 2100\}$ ,  $m \in \mathbb{M} = \{1, 2, N\}$ , and  $e \in \mathbb{S}_{e,\text{test}} = \{\text{ssp245}\}$ . The ClimateBench dataset has  $N = 3$  realizations. The sums over those sets are abbreviated as  $\sum_{\text{index} \in \text{set}} =: \sum_{\text{index}}$ . We summarize the climate variables by denoting the tensors  $\mathbf{Y}_e = \{y_{i,j,t,m,e}\}_{i \in \mathbb{I}, j \in \mathbb{J}, t \in \mathbb{T}_{\text{test}}, m \in \mathbb{M}}$  and  $\hat{\mathbf{Y}}_e = \{\hat{y}_{i,j,t,e}\}_{i \in \mathbb{I}, j \in \mathbb{J}, t \in \mathbb{T}_{\text{test}}}$ . In general, we denote a tensor as  $\mathbf{A}$ , matrix as  $\mathbf{A}$ , set as  $\mathbb{A}$ , cardinality of a set as  $|\mathbb{A}|$ , and scalar as  $a$ .

## 2.2 Em-MPI data: Addressing internal variability with the MPI-ESM1.2-LR ensemble

We select the MPI-ESM1.2-LR (v1.2.01p7) (Mauritsen et al., 2019) single model initial-condition large ensemble (Olonscheck et al., 2023) for extracting the data subset, *Em-MPI*. We choose the MPI model instead of other climate models, by first subselecting the CMIP6 models from the multi-model large ensemble archive, MMLEAv1 by Deser et al. (2020), that ran at least 30 realizations by 2022/12/01 for the Tier 1 scenarios in ScenarioMIP (ssp126, -245, -370, and -585). This leaves only three models: MPI-ESM1.2-LR, EC-Earth3, and CanESM5. We choose the MPI model for its transient climate response within the “likely” range and near-immediate availability of all realizations, though other reasonable choices exist (see Appendix B2). Further, MPI-ESM1.2-LR simulates internal variability in surface temperature comparable to observations and only slightly underestimates the variability in precipitation (Olonscheck et al., 2023).

The Em-MPI dataset contains 50 realizations for each emission scenario, which can be used to average out or reduce the interannual fluctuations from internal variability and extract the emission-forced signal as illustrated in Fig. 2 and Section 3.2.1. We download the 50 realizations for annual mean surface temperature and precipitation for the scenarios  $\mathbb{S}_e^{\text{em-mpi}} = \{\text{ssp126}, \text{ssp245}, \text{ssp370}, \text{ssp585}, \text{historical}\}$  at T63 horizontal resolution ( $\approx 1.8^\circ$  or 180km;  $96 \times 192$  pixels). We do not regrid this dataset. Each ssp and historical scenario contains  $T_{\text{ssp}} = 86$  or  $T_{\text{hist}} = 165$  years, respectively. We compute anomalies by taking each annually-averaged variable and subtracting the preindustrial climatology, i.e., the locally-resolved average over a 400-year preindustrial control run during year 1450 to 1850.

As hourly precipitation rates are approximately log-normally distributed (Cho et al., 2004), it might be desirable to download hourly instead of annually-averaged precipitation and take a log transform of precipitation before computing ensemble and annual averages. However, we maintain precipitation in its original scale to keep results comparable between the Em-MPI and NorESM2-LM targets and because annually-averaged precipitation is a well studied quantity. Furthermore, we do not take the log of annually-averaged precipitation anomalies because, consistent to the central limit theorem, their distribution more closely resembles a Gaussian rather than a log-normal (Fig. B3 shows the actual distribution).

## 2.3 Linear Pattern Scaling emulator

Linear Pattern Scaling (LPS) is a commonly used emulation technique to analyse regional climate change as a function of global emissions (Mitchell et al., 1999; Giorgetta et al., 2013); see review by Lee et al. (2021). In our LPS emulator,  $\hat{f}_{\text{LPS}}$ , a linear regression fit first relates scalar global cumulative CO<sub>2</sub> emissions,  $x_{t,e} = \text{CO}_{2;t,e}^{\text{cum}} \in \mathbb{R}$ , to global surface temperature anomalies,  $\bar{T}_{t,e}^{\text{surf}} \in \mathbb{R}$ , for a chosen year,  $t \in \{1850, 1851, \dots, 2100\}$ , and emission scenario,  $e \in \mathbb{S}_e$ :

$$\hat{\bar{T}}_{t,e}^{\text{surf}} = w^{\text{global}} x_{t,e} + b^{\text{global}}. \quad (3)$$

This regression for global temperature does not utilize other emission variables consistent with the evidence that  $\bar{T}_{t,e}^{\text{surf}}$  is predominantly linearly proportional to  $\text{CO}_{2;t,e}^{\text{cum}}$  (see (MacDougall, 2016) and Fig. 3-left). Many techniques emulate the global mean temperature more accurately than a linear fit, for example, by considering non-CO<sub>2</sub> forcings or multiple time-scales (Meinshausen et al., 2011; C. J. Smith et al., 2018), but we are choosing to sacrifice accuracy for added simplicity and interpretability.

Then, we fit local linear regression functions independently for each grid cell,  $(i, j)$ , to map global temperature anomalies onto the local climate variable of interest,  $y_{i,j,t,e} \in \mathbb{R}$ :

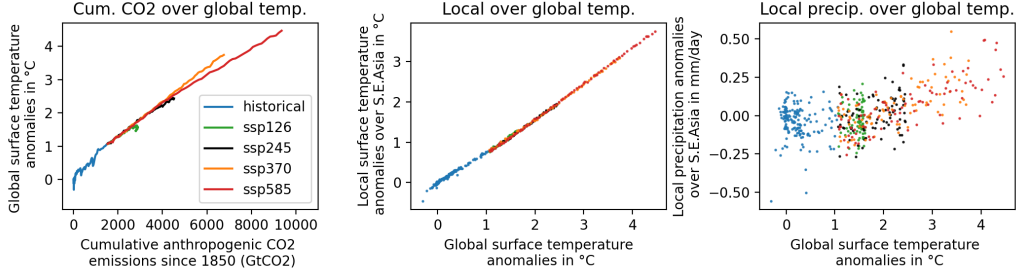


Figure 3: **Functional relationships in cumulative CO<sub>2</sub> emissions, surface temperature, and precipitation.** The left plot shows the almost linear relationship between cumulative CO<sub>2</sub> emissions (x-axis) and global ensemble-mean surface temperature anomalies (y-axis) for each scenario in the Em-MPI data. The middle and right plot show the ensemble-mean local surface temperature and precipitation anomalies, respectively, averaged over each year (dot) and the IPCC AR6 region S.E.Asia, against the annually-averaged global surface temperature anomaly. We selected S.E.Asia to highlight the contrast between linear and more complex relationships in temperature vs. precipitation and show other regions in Fig. C6.

$$\hat{y}_{i,j,t,e} = w_{i,j}^{\text{local}} \hat{T}_{t,e}^{\text{surf}} + b_{i,j}^{\text{local}} \quad (4)$$

This regression assumes that any local climate variable can be described as a linear function of the global mean temperature and that this function is consistent across emission scenarios. This assumption is known to be relatively accurate for local surface temperature and less accurate for local precipitation (see (Tebaldi & Arblaster, 2014) and Fig. 3-middle and -right). The existing implementation of LPS on ClimateBench (Watson-Parris et al., 2022) uses  $\bar{T}_{t,e}^{\text{surf}}$  from the target dataset as inputs (instead of estimating the variable from emissions). Our LPS emulator can be represented as matrix operations:  $\hat{\mathbf{Y}}_{t,e} = \hat{f}_{\text{LPS}}(x_{t,e}) = \mathbf{W}^{\text{local}}(w^{\text{global}}x_{t,e} + b^{\text{global}}) + \mathbf{B}^{\text{local}}$  with  $\hat{\mathbf{Y}}_{t,e} = \{\hat{y}_{i,j,t,e}\}_{i \in \mathbb{I}, j \in \mathbb{J}}$ . The LPS emulator including the global and local weights and intercepts,  $w^{\text{global}}, b^{\text{global}}, w_{i,j}^{\text{local}}, b_{i,j}^{\text{local}} \in \mathbb{R}$ , are independent of time and scenario. We split the global and local regression into Eqs. (3) and (4) for interpretability, but adding a global weight and intercept is redundant; thus, the total number of free parameters is the number of local weights and intercepts:  $2 * I * J$ . By construction, LPS preserves the global average if the local variable and the global variable are both temperature (Sect.2.2 in Wells et al. (2023)). The optimal weights are found via ordinary least squares with the Python package scikit-learn (Pedregosa et al., 2011).

## 2.4 Review of the CNN-LSTM emulator

A CNN-LSTM is a commonly used neural network architecture for learning spatiotemporal correlations (Shi et al., 2015) and has been evaluated by Watson-Parris et al. (2022) on ClimateBench. In comparison to LPS, the CNN-LSTM is expected to be capable of learning more complex functions by having more free parameters. The CNN-LSTM also contains a 10-year memory and incorporates all emission variables, including spatially resolved aerosols, as inputs.

To increase the comparability between the CNN-LSTM scores on the Em-MPI and NorESM data, we follow the implementation in the ClimateBench paper as closely as possible. This includes using the same hyperparameters, because the reference implementation did not withhold any samples for validation and did not go through the process of hyperpa-

parameter optimization. However, we noticed that the CNN-LSTM converges to significantly different minima depending on the weight initialization random seed. To compensate for this spurious dependence on initialization, we deviate from the original implementation by training the CNN-LSTM multiple times with different weight initialization random seeds and reporting the average scores across those seeds whenever we evaluate the CNN-LSTM. We also terminate the CNN-LSTM training process when the test error stops improving to reduce computational cost and avoid memorization of the training data. See Appendix B3 for details on this CNN-LSTM.

## 2.5 Testing the influence of internal variability on emulator performance

We construct the following experiment to quantify the impact of internal variability on emulator performance (with results in Fig. 5 and Section 3.2.2). We fit two emulation techniques (LPS and CNN-LSTM) on random ensemble subsets of  $n$  realizations and evaluate them for each  $n$  on the mean of all 50 realizations. We evaluate on the mean of 50 (instead of  $n$ ) realizations, because we aim to benchmark emulators of the forced mean climate response (Maher et al., 2019). We assume that 50 realizations are sufficient to approximate the true forced climate response of a given climate model, which is a reasonable assumption for most variables and spatiotemporal resolutions (Tebaldi et al., 2021; Olonscheck et al., 2023). Thus, evaluating against the mean of 50 realizations will determine for each  $n$ -member training set which technique we define as the ‘‘better’’ emulator for the MPI-ESM1.2-LR model. We use ‘member’ and ‘realization’ interchangeably.

In detail, we randomly draw the ensemble subsets,  $\mathbb{M}_{n,k} \subset \mathbb{M} = \{1, 2, \dots, N^{\text{em-mpi}}\}$ , where  $n = |\mathbb{M}_{n,k}|$  denotes the number of realizations in a subset,  $k$  indexes the  $k$ th random draw of equally sized subsets, and  $m \in \mathbb{M}_{n,k}$  is the realization ID. Each ensemble subset is drawn from the Em-MPI data that has  $N^{\text{em-mpi}} = 50$  realizations without replacement, i.e., within each subset there are no duplicate realization IDs. To compensate for the variation across subsets, we draw  $K = 20$  ensemble subsets of the same size for every  $n$  and report the mean and standard deviation. The subsets, for example, contain the realization IDs,  $\mathbb{M}_{1,1} = \{3\}, \mathbb{M}_{1,2} = \{48\}, \dots, \mathbb{M}_{3,1} = \{2, 18, 36\}, \mathbb{M}_{3,2} = \{1, 10, 42\}$ , etc.

We fit each emulation function,  $\hat{f}_{\text{LPS}}$  and  $\hat{f}_{\text{CNN-LSTM}}$ , on the ensemble-mean of each ensemble subset,  $\mathbb{E}_{\mathbb{M}_{n,k}}[\mathbf{Y}_{\text{train}}] = \frac{1}{|\mathbb{M}_{n,k}|} \sum_m \mathbf{Y}_{m,\text{train}}$ , and denote the fitting or training process with a  $P$ . We use the same inputs as in ClimateBench, targets from the Em-MPI data, and a train/test data split equivalent to the one in ClimateBench, i.e.,  $\mathbb{S}_{e,\text{train}}^{\text{em-mpi}} = \{\text{historical, ssp126, ssp370, ssp585}\}$  and  $\mathbb{S}_{e,\text{test}}^{\text{em-mpi}} = \{\text{ssp245}\}$  with  $\mathbb{T}_{\text{test}} = \{2080, 2081, \dots, 2100\}$ ,  $\mathbf{X}_{\text{train}} = \{\mathbf{X}_e\}_{e \in \mathbb{S}_{e,\text{train}}^{\text{em-mpi}}}$ , and  $\mathbf{Y}_{\text{train}} = \{\mathbf{Y}_e\}_{e \in \mathbb{S}_{e,\text{train}}^{\text{em-mpi}}}$ . After training, we evaluate the emulators on the ensemble-mean of all 50 realizations,  $\mathbb{E}_{\mathbb{M}}[\mathbf{Y}_{\text{test}}]$ . As evaluation metrics, we use the spatial and global  $\text{RMSE}_*$  (from Eqs. (1) and (2)), averaged over the ensemble subsets, and the difference between the emulator scores,  $\Delta \text{RMSE}_{*,n} = \text{RMSE}_{*,n,\text{CNN-LSTM}} - \text{RMSE}_{*,n,\text{LPS}}$ . The train and evaluation process is conducted independently for precipitation and surface temperature. In summary:

$$\hat{f}_{n,k} \stackrel{\text{fit}}{\leftarrow} P[\mathbf{X}_{\text{train}}, \mathbb{E}_{\mathbb{M}_{n,k}}[\mathbf{Y}_{\text{train}}]] \quad (5)$$

$$\text{RMSE}_{*,n} = \frac{1}{K} \sum_{k \in \{1, \dots, K\}} \text{RMSE}_* \left( \hat{f}_{n,k}(\mathbf{X}_{\text{test}}), \mathbb{E}_{\mathbb{M}}[\mathbf{Y}_{\text{test}}] \right) \quad (6)$$

We use the LPS and CNN-LSTM as described in Sections 2.3 and 2.4, respectively. We train the CNN-LSTM  $L = 20$  times with different weight initialization random seeds per realization subset draw and use the average RMSEs of those 20 seeds as the scores for a given subset draw, as detailed in Eq. (B3). We fit the LPS emulator for every  $n \in \{1, 2, \dots, 50\}$  which results in  $K * 50 = 1000$  runs and the CNN-LSTM for  $n \in \{1, 2, \dots, 15, 16, 20, 25, 30, 40, 50\}$  resulting in  $L * K * 21 = 8400$  runs.

We report the spatial and global RMSE for training on the 50-member ensemble-mean targets in Table 2. We computed scores for LPS and the CNN-LSTM reimplementation, and we recommend scientists that add emulation techniques to clarify that “scores are computed on the Em-MPI targets using the ClimateBench evaluation protocol”.

## 2.6 A heuristic model to illustrate internal variability effects

To better understand why internal variability influences the emulator performance, we repeat the internal variability experiment on a simplified dataset. We generate the dataset with a one-dimensional nonlinear model that relates emissions to a hypothetical climate variable with internal variability. The model is based on an energy balance budget (e.g., Giani et al. 2024) that simulates temperature change as a function of cumulative emissions of a fictitious greenhouse gas, climate feedbacks, and noise. The noise is sampled from a Wiener process, representing internal variability generated by chaotic atmospheric dynamics (Hasselmann, 1976). Integrating the noise over time creates unpredictable high- and low-frequency fluctuations, comparable to interannual and (multi-)decadal oscillations (Frankignoul & Hasselmann, 1977). The hypothetical climate variable is an arbitrary nonlinear function of temperature, comparable to precipitation in the real climate system.

We use the ensemble-mean across  $n$  independent realizations of this model as one training set, and repeat this to generate  $K = 2000$  training sets for every  $n$ . We fit a neural network and a linear regression function to each training set and, in comparison to Section 2.5, train the fixed-complexity neural networks by following best practices to avoid overfitting, such as using a separate validation set and tuning regularization parameters. After training, we evaluate both emulation techniques using the expected MSE for every  $n$  with respect to the noise-free emission-forced signal. We detail the heuristic model and training process in Appendix D1.

Following the bias-variance decomposition, we decompose the MSE scores into a bias-squared and variance term,  $\text{MSE}_n = \text{Bias}_n^2 + \text{Var}_n$ , as proven in Appendix D2. This decomposition allows us to interpret each emulation technique in the context of the well-studied bias-variance tradeoff (Bishop, 2006). We also compute the expected Fourier spectra of the neural network and linear fits to identify if the methods are influenced by lower or higher frequency noise components.

## 3 Results

In Section 3.1, we quantify the performance of LPS on ClimateBench. For spatial precipitation, LPS achieves better scores than deep learning-based emulators even though the relationships are known to be nonlinear (discussed in Section 4.1). In Section 3.2, we illustrate that the internal variability in the 3-member ClimateBench targets is high in comparison to the 50-member Em-MPI data. Then, we illustrate that this high internal variability can skew benchmarking scores in favor of LPS, i.e., LPS often has comparatively better scores than the CNN-LSTM if there is more internal variability in the training set. Lastly, we explain this effect of internal variability by demonstrating the associated bias-variance tradeoff on a simplified dataset.

### 3.1 Evaluation of Linear Pattern Scaling on ClimateBench

#### 3.1.1 Regional accuracy of LPS

Figure 4 shows that LPS (middle) predicts surface temperature patterns that are similar to the ClimateBench test set targets (left). Important warming patterns are visible in the LPS predictions; for example, a North Atlantic “cold blob”, Arctic amplification, and proportionately higher warming over land and the Northern Hemisphere. Figure 4-right shows that LPS predicts the surface temperature anomalies in most regions within a  $\pm 0.25^\circ\text{C}$

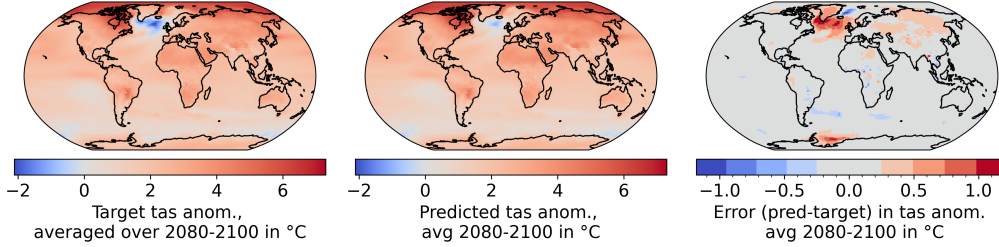


Figure 4: **Linear pattern scaling error map.** The left plot shows the target surface temperature anomalies (tas) from the ssp245 ClimateBench test set, which are averages over 3 realizations and 21 years (2080-2100). The middle plot shows the linear pattern scaling predictions and the right plot the error of predictions minus the target. The other variables are plotted in Figures C1 to C3.

error bar of the target ESM-simulated values. The global patterns in the LPS predictions also resemble the target patterns for other climate variables, as shown in Figs. C1 to C3. Limitations of LPS are visible in regional errors, for example, in the surface temperature at the North Atlantic cold blob and Weddell Sea. These errors could arise from nonlinear relationships or internal variability, as discussed in existing LPS evaluations (Wells et al., 2023) and Section 4.1.

### 3.1.2 Quantitative comparison of LPS with deep learning emulators

Table 1 compares LPS against all other emulators that have reported scores on ClimateBench including the transformer-based foundation model, ClimaX, with 108M free parameters that is currently being cited as the best performing emulator (Kaltenborn et al., 2023). The Gaussian Process and Random Forest entries are described in (Watson-Parris et al., 2022). The CNN-LSTM by (Watson-Parris et al., 2022) is summarized in Appendix B3, CNN-LSTM (reproduced) is reimplement of this CNN-LSTM by (Nguyen et al., 2023), and Cli-ViT is a vision transformer detailed in (Nguyen et al., 2023). We highlight the emulator with the lowest NRMSE score (i.e. best performance) in **bold**. But, we caution the reader not to draw a definitive conclusion which emulation technique is most accurate beyond the ClimateBench benchmark because of the internal variability in the NorESM2-LM targets, as analysed in Section 3.2.

LPS has the lowest spatial NRMSE scores for 3 out of 4 variables including surface temperature, precipitation, and 90th percentile precipitation (see Table 1). Further, LPS requires 4 orders of magnitude fewer parameters than ClimaX. This result implies that LPS is the new incumbent on spatial variables, i.e., the emulation technique that achieves the lowest score in the most “Spatial” columns, on ClimateBench.

ClimaX and the CNN-LSTM (reproduced) have better scores than LPS on diurnal temperature range, which is strongly influenced by aerosols, as discussed in (Watson-Parris et al., 2022). ClimaX and CNN-LSTM (reproduced) also have better global scores in precipitation and 90th percentile precipitation which we discuss in Appendix C5. Giving every column in the results table equal weight, LPS and ClimaX are on par with each other with each having better scores on 6 out of 12 columns.

LPS outperforming deep learning on surface temperature aligns with the domain intuition that there is a linear relationship to cumulative CO<sub>2</sub> emissions. But, it is surprising that LPS also outperforms the nonlinear deep learning-based emulators on spatial precipitation even though the relationships are known to be nonlinear.

Table 1: **ClimateBench results table including linear pattern scaling.** Spatial, Global, and Total denote normalized root mean square errors (NRMSEs) as detailed in Eqs. (1), (2) and (B1). The standard deviation of the three target ensemble members is denoted as Target std. dev. (WP22). We use three significant digits unless reported otherwise in the reference(*t*). The references are WP22 (Watson-Parris et al., 2022) and N23 (Nguyen et al., 2023).

	ref.	#param	Surface temperature			Diurnal temperature range			Precipitation			90 <sup>th</sup> percentile precipitation		
			Spatial	Global	Total	Spatial	Global	Total	Spatial	Global	Total	Spatial	Global	Total
Gaussian process	WP22	n/a	0.109	0.074 <sup>t</sup>	0.478	9.21	2.68	22.6	2.34	0.341	4.05	2.56	0.429	4.70
CNN-LSTM	WP22	365K	0.107	0.044 <sup>t</sup>	0.327	9.92	1.38	16.8	2.13	0.209	3.18	2.61	0.346	4.34
CNN-LSTM (reproduced)	N23	365K	0.123	0.080 <sup>t</sup>	0.524	7.47	1.23	13.6	2.35	<b>0.151</b>	<b>3.10</b>	3.11	<b>0.282</b>	4.52
Random forest	WP22	47.5K	0.108	0.058 <sup>t</sup>	0.4 <sup>t</sup>	9.20	2.65	22.5	2.52	0.502	5.04	2.68	0.543	5.40
Cli-ViT	N23	unavail.	0.086 <sup>t</sup>	0.044 <sup>t</sup>	0.305	7.00	1.76	15.8	2.22	0.241	3.43	2.80	0.329	4.45
ClimaX	N23	108M	0.085 <sup>t</sup>	0.043 <sup>t</sup>	0.297	<b>6.69</b>	<b>0.810</b>	<b>10.7</b>	2.19	0.183	3.11	2.68	0.342	4.39
Linear pattern scaling	ours	27.7K	<b>0.0786</b>	<b>0.0410</b>	<b>0.284</b>	8.02	2.15	18.8	<b>1.87</b>	0.268	3.20	<b>2.25</b>	0.357	<b>4.03</b>
Target std. dev.	WP22	-	0.052 <sup>t</sup>	0.072 <sup>t</sup>	0.414	2.51	1.49	9.97	1.35	0.268	2.69	1.76	0.457	4.04

### 3.2 Analysing the relationship between internal variability and performance assessments of climate emulators

In this section, we analyse if internal variability contributes to the comparatively good scores of LPS on the ClimateBench spatial precipitation. We cannot conduct our internal variability experiment on the ClimateBench targets, because the experiment requires many ensemble members. Thus, we first demonstrate the magnitude of internal variability in the ClimateBench targets in comparison to the Em-MPI targets. Then, we show that the magnitude of internal variability in the targets affects the benchmark scores using the Em-MPI data and explain this influence using a simplified dataset. This suggests that internal variability can impact benchmark scores on any dataset that does not contain enough members to average out internal variability, including the ClimateBench dataset, as discussed in Section 4.3.

#### 3.2.1 Magnitude of internal variability in 3-member NorESM2-LM and 50-member MPI-ESM1.2-LR ensemble average

Figure 2 illustrates the magnitude of internal variability in the 3-member NorESM2-LM targets in comparison to the 50-member MPI-ESM1.2-LR targets. First, Fig. 2a shows the ensemble-mean surface temperature anomalies over time for the NorESM (left) and Em-MPI (middle) data. The anomalies are plotted as a global-average (black) and regional-average over a sample region (red). Interannual fluctuations from internal variability are still visible in the global NorESM (left,black) data and are higher at the regional scale, exemplified by fluctuations up to  $\pm 1.5^{\circ}C$  over the Greenland/Iceland region (left,red). Similar plots in Fig. 2b illustrate that internal variability is even higher for precipitation and dominates the signal on a regional scale, here over S. Central-America.

The 50-member mean in the Em-MPI data (middle) shows notably lower fluctuations from internal variability for temperature and precipitation. Figure C4 shows that the fluctuations from internal variability also seem lower across a diverse set of regions. Additionally, we plot averages over a 21-year sliding window in Fig. C4, because the spatial RMSE in Eq. (1) computes a 21-year average before calculating the spatial errors. In most regions, the fluctuations in the 21-year averaged precipitation are also visibly lower in comparison to the NorESM2-LM ensemble-mean.

#### 3.2.2 Effect of internal variability on benchmark scores

Figure 5-top shows the results of our internal variability experiment for precipitation anomalies from the Em-MPI data. When high internal variability is present in the training

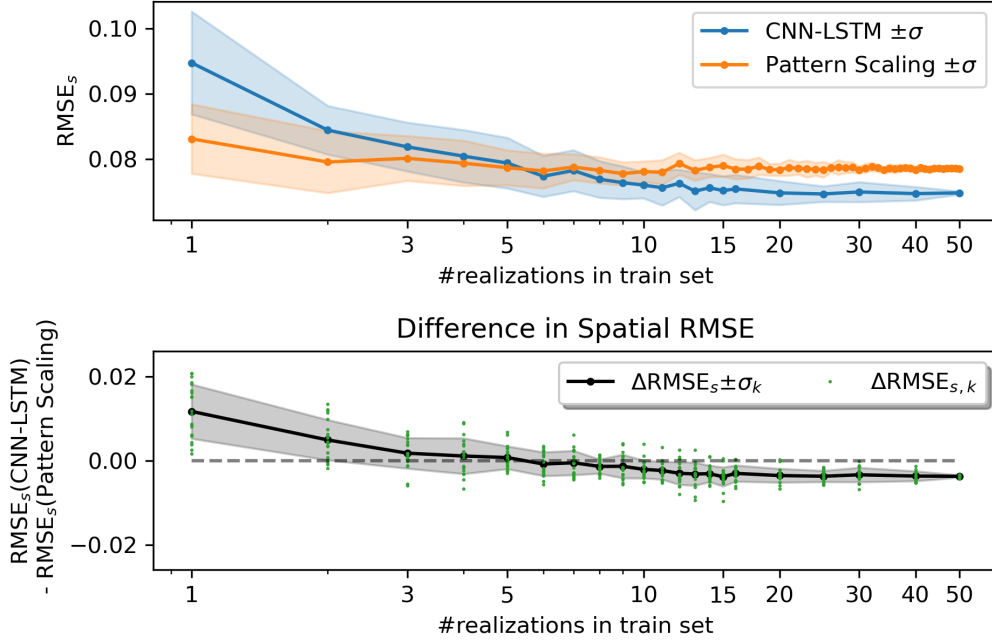


Figure 5: **Error over realizations in training set for precipitation in mm/day.** The top figure in our internal variability experiment shows the spatial RMSE, i.e.,  $\text{RMSE}_{s,n}$ , of an LPS (orange) and CNN-LSTM emulator (blue) that were trained on the ensemble-mean of data subsets with  $n$  realizations and evaluated on the ensemble-mean of  $N = 50$  realizations from the Em-MPI data. Shading indicates the standard deviation across  $K = 20$  random draws of realization subsets. The bottom figure shows the difference in spatial RMSE, i.e.,  $\Delta\text{RMSE}_{s,n}$ , between the two emulators for each random realization subset,  $(n, k)$ , (green dots); and the mean and standard deviation across  $K$  subsets (black line and shading). Data is plotted on a log x-axis, because most climate models are run for 1 to 10 realizations per scenario. As a side note, the  $\pm\sigma$  range in the bottom figure is not the average of the two  $\sigma$  ranges in the top figure, because an emulator’s RMSE covaries with the subset, i.e., if one emulator has low RMSE the other emulator is also likely to have low RMSE.

set at  $n = 3$  realizations, the LPS (orange) has a better spatial RMSE than the CNN-LSTM (blue). This mirrors the results on the ClimateBench results table in Table 1. As the internal variability is increasingly averaged out by including more realizations in the training data set, the RMSE of the CNN-LSTM decreases. The LPS and CNN-LSTM RMSEs become comparable at  $n = 6$  realizations. For more realizations up to 50 the CNN-LSTM has a better score than the LPS. This trend is also visible when plotting the difference,  $\Delta\text{RMSE}_s(n)$ , which is positive at  $n = 3$  and crosses the zero-intercept at  $n \approx 6$  in Fig. 5-bottom.

We illustrate that high internal variability skews the benchmarking scores towards a lower complexity emulator by fitting a linear trend to  $\Delta\text{RMSE}(n)$  and observing a negative slope. The linear fits are shown in Fig. C5 and have a slope of  $-5.77 \times 10^4$  for spatial precipitation and a slope of  $-12.2 \times 10^4$  for spatial surface temperature. We fit the linear trend only over the x-axis inset  $n \in [0, 20]$ , because the subsets contain an increasing number of duplicates across  $n$ , which increasingly flattens out the slope even if there is still leftover internal variability, a known issue of ensemble analyses (Tebaldi et al., 2021).

Figure 5-bottom also shows that there is at least one realization subset with 3 realizations that has  $\Delta\text{RMSE}_s < 0$  (green dot below zero line). This implies that on some

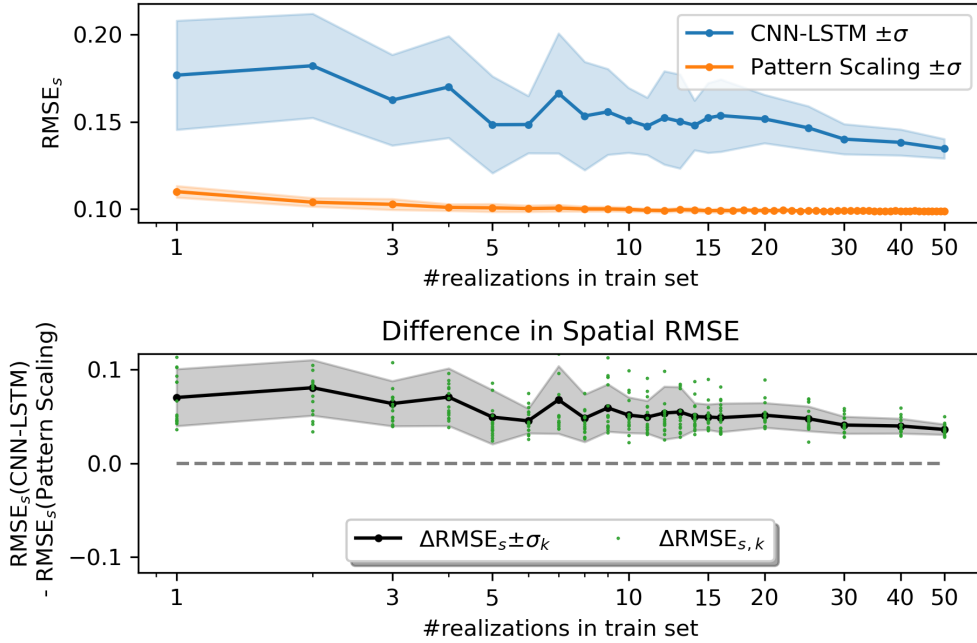


Figure 6: **Error over realizations in training set for surface temperature °C.** The LPS emulator (top-plot, orange) has a lower spatial RMSE on surface temperature in comparison to the CNN-LSTM (blue) independent of the number of realizations in the training set. The difference between both emulation techniques slightly decreases, but the scores between different subsets (bottom-plot, green dots) have significant spread.

Table 2: **Em-MPI results table.** Spatial and global RMSE, following Eqs. (1) and (2), using the Em-MPI 50-member ensemble-mean as targets and the ClimateBench evaluation protocol. The scores contain three significant digits.

	#param	Surface temperature		Precipitation	
		Spatial	Global	Spatial	Global
CNN-LSTM	485K	0.135	0.0679	<b>0.0748</b>	0.0152
Linear pattern scaling	36.8K	<b>0.0989</b>	<b>0.0265</b>	0.0785	0.0152

3-member subsets from the MPI-ESM1.2-LR model, CNN-LSTM outperforms LPS on spatial precipitation. And, this suggests that a lucky random draw of three realizations for the ClimateBench NorESM2-LM spatial precipitation targets could have also lead to a flipped result where the CNN-LSTM outperforms LPS.

For surface temperature, plotted in Fig. 6, the LPS emulator achieves better spatial RMSE scores than the CNN-LSTM independent of the number of realizations in the training set. The RMSE scores at  $n = 50$  are given in Table 2. Similar to precipitation, the difference between LPS and CNN-LSTM (shown in Fig. 6-bottom) decreases with increasing number of realizations in the training set although with a negative slope of lower magnitude. These results would be in line with an expectation that surface temperature contains less internal variability than precipitation and is thus averaged out with fewer climate realizations (Tebaldi et al., 2021). Further, these results are consistent with our expectation

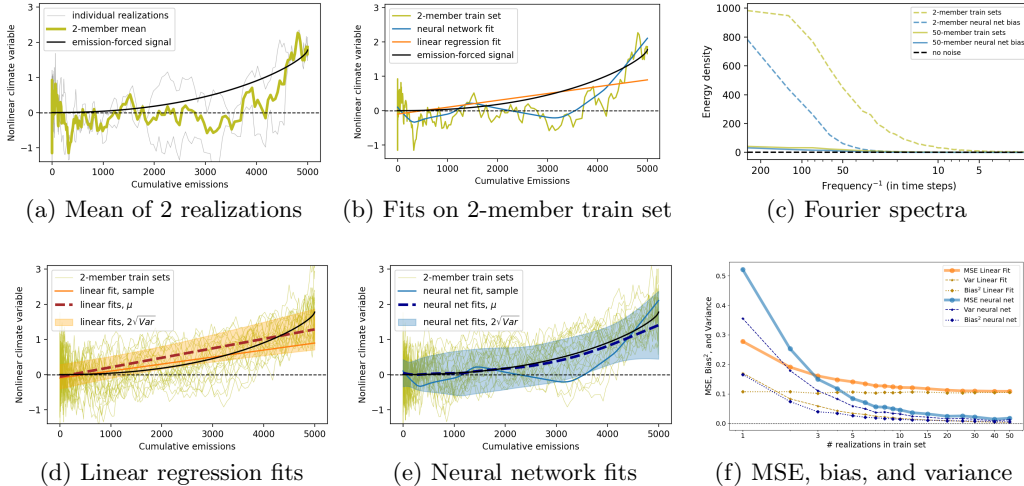


Figure 7: **Bias-variance trade-off on a simplified dataset.** Figure 7a shows two realizations (gray lines), the corresponding ensemble-mean (olive), and the emission-forced signal (black) of an idealized one-dimensional stochastic function. The best neural network (blue) and linear (orange) fit to this 2-member ensemble-mean are plotted in Figure 7b. Figures 7d and 7e show the mean and variance of each emulation technique across 500x draws of a 2-member ensemble-mean, illustrating a comparatively higher variance across neural network fits. Figure 7c shows the expected Fourier spectra of an  $n$ -member average of the underlying noise process and the corresponding signal-removed neural network fits, according to Eq. (D3). Figure 7f plots the expected variance (star-dashed), bias<sup>2</sup> (diamond-dashed), and MSE (shaded line) of each emulation techniques as a function of members in the ensemble-mean training sets.

given the predominantly linear relationship of surface temperature with cumulative CO<sub>2</sub> emissions.

### 3.2.3 Explanation of overfitting and the bias-variance tradeoff

The comparatively worse performance of a deep learning emulator in the noisy data regime (low  $n$ ) can be explained on the simplified dataset. Figure 7b illustrates that a neural network fit (blue) can be influenced by the low-frequency variability in a training set that only contains 2 members (olive). Plotting the Fourier spectra of neural net biases (blue) and the noise-process (olive) in Fig. 7c shows that the neural network fits on 2-member training sets maintain some energy from the noise process at lower frequencies, while filtering out higher frequency noise. If a neural network would have accurately filtered out all noise, the energy density would be close to zero in this plot (see 50-member fits). This shows that emulation techniques can overfit to noise in the training data, noting that the range of overfitted frequencies should vary depending on the number of free parameters and regularization techniques.

The bias-variance tradeoff gives an explanation why the highest-scoring emulation technique switches as a function of  $n$ : When there is significant noise in the training set there is more variance between different neural network fits than linear fits, as illustrated with 2-member sets in Figs. 7d and 7e. Plotting the variance over  $n$  in Fig. 7f confirms this quantitatively and shows that the variance (purple, star-dashed) is the major contributor to the neural networks' MSE score (blue, solid) at  $n=2$ . The linear fits have lower variance at  $n=2$  (brown, star-dashed), but also take a strong assumption on the functional form

and, thus, have a significant bias (diamond-dashed, brown). As the number of realizations in the training set increases, the bias of the linear fits stays constantly high whereas the neural networks' variance decreases. This causes a switch of the emulator with the lower MSE score at  $\sim 3$  realizations, similar to the switch of the higher scoring emulator on the Em-MPI spatial precipitation targets.

The bias-variance tradeoff also explains the effect of regularization. In this case, the neural network is regularized causing a non-zero bias (diamond-dashed, brown). But, re-training the neural network without regularization would result in a zero bias and higher variance, e.g., at  $n = 2$  (Bishop, 2006).

## 4 Discussion

### 4.1 Importance of comparing with an LPS baseline

Our analysis indicates that quantitative comparisons with LPS can help determine if deep learning-based emulators are making meaningful progress on known issues in climate emulation. For example, it is known that the relationships between global annual mean surface temperature vs. cumulative CO<sub>2</sub> emissions (MacDougall, 2016) and local vs. global annual mean surface temperature (Tebaldi & Arblaster, 2014) are predominantly linear and these relationships could be seen as minimum criteria for validating deep learning-based emulators. Deep-learning-based emulators may hold more promise for emulating settings that are known limitations of LPS, such as emulating overshoot scenarios, daily statistics and hourly dynamics, abrupt transitions, or extremes in regions with narrow temperature distributions (Womack et al., 2025; MacDougall, 2016; Wells et al., 2023; Tebaldi et al., 2020). Further, nonlocal aerosols (Levy II et al., 2013; Williams et al., 2022, 2023), short-term effects of CO<sub>2</sub> (Cao et al., 2015), or convection over tropical oceans (Kravitz et al., 2017) can impact precipitation nonlinearly. Theoretical insights on the limitations of linear emulators can be found in literature surrounding the fluctuation-dissipation theorem (Leith, 1975; Lembo et al., 2020) and an analysis by Giani et al. (2024). Our work has shown that a deep learning-based emulator can improve marginally on LPS for emulating the Em-MPI spatial precipitation targets (see Table 2). However, many nonlinear phenomena remain to be studied to determine if advanced emulation techniques could improve on LPS baselines.

Generally speaking, our study emphasizes the importance of benchmarking machine learning (ML)-based emulators against established techniques. While the allure of novel ML approaches is understandable, it is not a good reason to neglect well-developed methods such as LPS. Neglecting well-developed methods may lead to an overestimate ML's skill, such as in the case of transformer-based emulators being cited as the most accurate emulators of surface temperature. Our work serves as a cautionary tale, highlighting the possibility of overlooking simpler techniques that may achieve comparable or superior performance.

### 4.2 Overfitting to internal variability and the bias-variance trade-off

Our results have shown that the highest-scoring emulation technique (LPS vs. CNN-LSTM) can change depending on the number of realizations (see Fig. 5). This is perhaps surprising if the underlying relationship is nonlinear in which case a CNN-LSTM would be expected to outperform a linear model (Bishop, 2006). But, using the simplified dataset in Fig. 7, we have shown that a deep learning-based emulator can also have comparatively high variance, leading to the emulator overfitting to low-frequency variability. And, if this variance outweighs the bias that is introduced through assuming a linear relationship, then linear regression can be the better scoring emulation technique to nonlinear functions.

This indicates that a general-purpose technique for emulating any variable of any ESM would need to be flexible in trading off bias and variance. In particular, this becomes relevant in the low-data regime, which can be the case for ESMs that only contain a few realizations

per scenario and climate variables, such as the change in surface winds, that have a low signal-to-noise ratio. Neural networks are a universal function approximator and, thus, appealing as general-purpose technique. But, at least in the case of our simplified dataset, standard methods of using weight decay and early stopping were insufficient to prevent neural networks from overfitting to low-frequency variability in this low-data regime. Thus, we recommend to additionally regularize emulation techniques through climate science-driven assumptions on the functional form and emulator’s complexity. Testing out various assumptions can be part of a hyperparameter optimization process that is conducted per-variable, per-ESM, recognizing that the highest scoring complexity may be quite simple.

It is an open question which choice of validation set would be the most practical for identifying this optimal complexity in future climate emulation benchmarks. In our internal variability experiment, we did not withhold a validation set for consistency with ClimateBench. For a future climate emulation benchmark with a small number of emission scenarios (e.g., 5) an alternative option would be to use a strategy of cross-validation similar to (Bouabid et al., 2024): train on 3 and validate on 1 scenario, optimize the hyperparameters on all 3:1 combinations of scenarios, test the model on 1 completely held out scenario, and repeat the steps for all held out scenarios that may be of scientific interest. Nevertheless, when only a few realizations per scenario are available it continues to depend on each climate variable’s signal-to-noise ratio if the set of all realizations across all scenarios contains sufficient information for distinguishing random low-frequency fluctuations, such as multidecadal oscillations, from long-term emission-forced signals, independent of how the validation set is chosen.

### 4.3 Limitations and applicability of our results

The difference in spatial precipitation RMSE between the two emulation techniques is relatively low ( $|\Delta\text{RMSE}_s| < 0.015\text{mm/day} \forall n \in \{1, \dots, N\}$ ). In this context, we note that justifications to switch from LPS to a deep learning-based emulator will depend on the application and likely require additional application-oriented evaluation metrics. But, independent of the error magnitude, our work shows that reporting the difference on an average of 50 instead of 3 realizations will give a more robust estimate of an emulator’s accuracy.

While we illustrated the impact of internal variability only on emulators of spatial patterns of temperature and precipitation in the MPI-ESM1.2-LR model, we expect similar results to apply to many other variables and models. In particular, we would expect that the benchmark scores on the NorESM2-LM 3-member mean spatial precipitation targets are also affected by internal variability due to the illustrated high magnitude of internal variability. Further, regionally-resolved near-surface wind velocities, for example, are known to have higher internal variability and a lower signal-to-noise ratio than precipitation which would raise the risk of overfitting. In general, if an emulation technique with high model complexity is overfitting when trained on the average of a few  $n$  realizations (which is not given), we would expect a downward trend in  $\Delta\text{RMSE}_s(n)$  with increasing  $n$  (as in Fig. 5-bottom and Fig. 6-bottom), although, the curvature and zero-intercept (if any) would change as a function of internal variability, linearity, and signal-to-noise ratio in the climate variable of interest.

To provide further empirical evidence for this relationship, LPS could also be compared with the deep learning-based emulation techniques in ClimateSet (Kaltenborn et al., 2023). ClimateSet is an alternative dataset for evaluating emulation techniques that is similar to ClimateBench, but uses monthly-averaged climate variables (tas, pr) and projections from multiple climate models as targets. As the test protocol in ClimateSet only uses a single realization per climate model, many of our results on ClimateBench likely also apply to ClimateSet. Unfortunately, the results in ClimateSet were not reproducible at the time of writing our paper (Kaltenborn et al., 2024), so we refer to future work for this comparison.

There are other ways of separating the forced response from internal variability beyond using more realizations and it would be interesting to study their relative advantages for assessing benchmarks. This becomes especially relevant for emulating high-resolution climate data ( $< 100km$ ) and scenarios for which models only contain a few realizations. For example, one can train or evaluate the emulator on variables averaged over a decadal time window. However, even a 30-year average can be insufficient to average out internal variability on a single climate realization (Maher et al., 2020). Alternatively, approaches from statistical learning (Sippel et al., 2019) or pattern recognition (Wills et al., 2020) are other promising avenues for extracting the forced target signal from emission scenarios with only few realizations.

## 5 Outlook and conclusion

Our work aims to improve the evaluation process of climate emulators by focusing on the impacts of internal variability. Besides internal variability, however, there are interesting directions towards improving climate emulation benchmarking (e.g., for ClimateBenchv2.0): First, additional scenarios, such as single forcer (4xCO<sub>2</sub>) or out-of-distribution (ssp119) experiments, could cover a less correlated input space and be used to evaluate an emulator’s capability to extrapolate beyond the training data. Second, the current evaluation metric, NRMSE, can be dominated by local extremes and only measures the accuracy of the predicted ensemble-mean. A future benchmark could add evaluation metrics that are more application-oriented (e.g., drought indices) or focus on assessing stochastic techniques, such as weather generators or diffusion models, that may aim to emulate the distribution of future climate states. A new benchmark could also include more diverse climate variables (e.g., highly varying regional winds or changes beyond 2100), a comparison with existing emulation techniques beyond LPS (e.g., (Beusch et al., 2022) or (Dorheim et al., 2023)), and a cross-validation strategy.

In conclusion, we showed that linear pattern scaling emulates the local annual mean temperature, precipitation, and extreme precipitation in ClimateBench more accurately than current deep learning emulators. We identified internal variability as a key reason for the comparatively good performance of linear pattern scaling on precipitation. This implies that addressing internal variability is necessary for benchmarking climate emulators. We assembled a data subset, Em-MPI, from the MPI-ESM1.2-LR ensemble that contains 50 instead of 3 realizations and can be used to augment the NorESM2-LM temperature and precipitation datasets in ClimateBench. Using the new dataset we showed that a CNN-LSTM can be more accurate for emulating precipitation, while linear pattern scaling continues to be the more accurate emulator for surface temperature anomalies, in terms of spatial RMSE scores.

## Reproducibility and data availability statement

The Em-MPI dataset is published with a CC-BY-4.0 license at [huggingface.co/datasets/blutjens/em-mpi](https://huggingface.co/datasets/blutjens/em-mpi). The code for reproducing all results is published at [github.com/blutjens/climate-emulator](https://github.com/blutjens/climate-emulator). The MPI-ESM1.2-LR data was retrieved from the Earth System Grid Federation interface (Wieners et al., 2019) under a CC-BY-4.0 license via the ESGF Pyclient API and building off the code in the ClimateSet downloader (Kaltenborn et al., 2023). The ClimateBench dataset was retrieved from (Watson-Parris, 2022) under a CC BY 4.0 license using the Python code in our github repository.

The internal variability experiment was implemented on a CPU cluster instead of GPUs, due to the parallelizability of the experiment and limited GPU availability; the experiment took a total of two weeks on 400 CPU cores. We used a mix of Intel Xeon Gold 6336Y (2.4GHz) and E5-2670 (2.6GHz).

## Author Contributions

B.L. is the lead author and contributed to all CRediT author roles except for funding acquisition. D. W.-P. contributed to conceptualization and writing - review and editing. R.F. and N.S. contributed to conceptualization, methodology, validation, resources, writing - review and editing, and funding acquisition.

## Acknowledgments

This project is supported by Schmidt Sciences, LLC and part of the MIT Climate Grand Challenges team Bringing Computation to the Climate Challenge (BC3).

Claudia Tebaldi has been instrumental for her insight on statistical analyses and existing literature in emulation. We are very grateful to Andre N. Souza, Paolo Gi-ani and the BC3 team members for regular methodological feedback and discussions regarding this work. We thank Konstantin Klemmer, Ruizhe Huang, Mengze Wang, and Chris Womack for their thorough pre-submission reviews and appreciate the dialogues with Iris de Vries and Shahine Bouabid. Thank you, to Dava Newman for the in-spirational support to start this line of work. Thank you, also to Katharina Berger for the rapid responses to support downloading the MPI data. We deeply appreciate the extensive feedback that we have received during the anonymous peer-review process.

## References

- Bassetti, S., Hutchinson, B., Tebaldi, C., & Kravitz, B. (2024, Jan.). *Diffesm: Conditional emulation of temperature and precipitation in earth system models with 3d diffusion models*. Retrieved from <https://doi.org/10.22541/essoar.170612214.43012845/v1>  
3
- Beusch, L., Gudmundsson, L., & Seneviratne, S. I. (2020). Emulating earth system model temperatures with mesmer: from global mean temperature trajectories to grid-point-level realizations on land. *Earth System Dynamics*, *11*(1), 139–159. Retrieved from <https://doi.org/10.5194/esd-11-139-2020>  
4
- Beusch, L., Nicholls, Z., Gudmundsson, L., Hauser, M., Meinshausen, M., & Seneviratne, S. I. (2022). From emission scenarios to spatially resolved projections with a chain of computationally efficient emulators: coupling of magicc (v7.5.1) and mesmer (v0.8.3). *Geoscientific Model Development*, *15*(5), 2085–2103. Retrieved from <https://doi.org/10.5194/gmd-15-2085-2022>  
18
- Bire, S., Lütjens, B., Azizzadenesheli, K., Anandkumar, A., & Hill, C. N. (2023). Ocean emulation with fourier neural operators: Double gyre. *Authorea, Inc.*. Retrieved from <http://dx.doi.org/10.22541/essoar.170110658.85641696/v1>  
3
- Bishop, C. M. (2006). *Pattern recognition and machine learning (information science and statistics)*. Berlin, Heidelberg: Springer-Verlag. Retrieved from <https://www.microsoft.com/en-us/research/uploads/prod/2006/01/Bishop-Pattern-Recognition-and-Machine-Learning-2006.pdf>  
10, 16
- Bouabid, S., Sejdinovic, D., & Watson-Parris, D. (2024). Fairgp: A bayesian energy balance model for surface temperatures emulation. *Journal of Advances in Modeling Earth Systems*, *16*(6). Retrieved from <https://doi.org/10.1029/2023MS003926>  
17
- Cao, L., Bala, G., Zheng, M., & Caldeira, K. (2015). Fast and slow climate responses to co2 and solar forcing: A linear multivariate regression model characterizing transient climate change. *Journal of Geophysical Research: Atmospheres*, *120*(23), 12,037–12,053.

Retrieved from <https://doi.org/10.1002/2015JD023901>

16

Cho, H.-K., Bowman, K. P., & North, G. R. (2004). A comparison of gamma and lognormal distributions for characterizing satellite rain rates from the tropical rainfall measuring mission. *Journal of Applied Meteorology*, *43*(11), 1586 - 1597. Retrieved from <https://doi.org/10.1175/JAM2165.1>

7

Deser, C., Lehner, F., Rodgers, K. B., Ault, T., Delworth, T. L., DiNezio, P. N., ... Ting, M. (2020, Apr 01). Insights from earth system model initial-condition large ensembles and future prospects. *Nature Climate Change*, *10*(4), 277-286. Retrieved from <https://doi.org/10.1038/s41558-020-0731-2> (data available at: <http://www.cesm.ucar.edu/projects/community-projects/MMLEA/>, last access: 03/2024)

7

Dorheim, K., Gering, S., Gieseke, R., Hartin, C., Pressburger, L., Shiklomanov, A. N., ... Bond-Lamberty, B. (2023). Hector v3.1.1: functionality and performance of a reduced-complexity climate model. *EGUsphere*, *2023*, 1–20. Retrieved from <https://doi.org/10.5194/egusphere-2023-1477>

3, 18

Dueben, P. D., Schultz, M. G., Chantry, M., Gagne, D. J., Hall, D. M., & McGovern, A. (2022). Challenges and benchmark datasets for machine learning in the atmospheric sciences: Definition, status, and outlook. *Artificial Intelligence for the Earth Systems*, *1*(3). Retrieved from <https://doi.org/10.1175/AIES-D-21-0002.1>

5

Eyring, V., Bony, S., Meehl, G. A., Senior, C. A., Stevens, B., Stouffer, R. J., & Taylor, K. E. (2016). Overview of the coupled model intercomparison project phase 6 (cmip6) experimental design and organization. *Geoscientific Model Development*, *9*(5), 1937–1958. Retrieved from <https://doi.org/10.5194/gmd-9-1937-2016>

5

Frankignoul, C., & Hasselmann, K. (1977). Stochastic climate models, part ii application to sea-surface temperature anomalies and thermocline variability. *Tellus*, *29*(4), 289-305. Retrieved from <https://doi.org/10.1111/j.2153-3490.1977.tb00740.x>

10

Giani, P., Fiore, A. M., Flierl, G., Ferrari, R., & Selin, N. E. (2024). *Origin and limits of invariant warming patterns in climate models*. Retrieved from <https://arxiv.org/abs/2411.14183>

3, 10, 16, 35

Gillett, N. P., Shiogama, H., Funke, B., Hegerl, G., Knutti, R., Matthes, K., ... Tebaldi, C. (2016). The detection and attribution model intercomparison project (damip v1.0) contribution to cmip6. *Geoscientific Model Development*, *9*(10), 3685–3697. Retrieved from <https://doi.org/10.5194/gmd-9-3685-2016>

5

Giorgetta, M. A., Jungclaus, J., Reick, C. H., Legutke, S., Bader, J., Böttinger, M., ... Stevens, B. (2013). Climate and carbon cycle changes from 1850 to 2100 in mpi-esm simulations for the coupled model intercomparison project phase 5. *Journal of Advances in Modeling Earth Systems*, *5*(3), 572-597. Retrieved from <https://doi.org/10.1002/jame.20038>

7

Goodfellow, I., Bengio, Y., & Courville, A. (2016). *Deep learning*. MIT Press. Retrieved from <http://www.deeplearningbook.org>

5

Hasselmann, K. (1976). Stochastic climate models part i. theory. *Tellus*, *28*(6), 473-485. Retrieved from <https://doi.org/10.1111/j.2153-3490.1976.tb00696.x>

10, 35

- Hausfather, Z., Marvel, K., Schmidt, G. A., Nielsen-Gammon, J. W., & Zelinka, M. (2022). Climate simulations: recognize the ‘hot model’ problem. *Nature Comment*, 605, 26-29. Retrieved from <https://doi.org/10.1038/d41586-022-01192-2>  
27
- Hawkins, E., & Sutton, R. (2009). The potential to narrow uncertainty in regional climate predictions. *Bulletin of the American Meteorological Society*, 90(8), 1095 - 1108. Retrieved from <https://doi.org/10.1175/2009BAMS2607.1>  
4
- Kaltenborn, J., Irvin, J., Saleem, H., Hasson, Y., & Lütjens, B. (2024, September 5). Response to ‘reproducing neurips paper fig. 6 results: predictions have no longitudinal dimension.’. Issue 12 in ClimateSet github repository. Retrieved from <https://github.com/RolnickLab/ClimateSet/issues/12#issuecomment-2332615137> (last accessed 11/19/2024)  
17
- Kaltenborn, J., Lange, C. E. E., Ramesh, V., Brouillard, P., Gurwicz, Y., Nagda, C., ... Rolnick, D. (2023, Jan). Climateset: A large-scale climate model dataset for machine learning. *Thirty-seventh Conference on Neural Information Processing Systems Datasets and Benchmarks Track*, 11(1), 1-3. Retrieved from <https://openreview.net/forum?id=3z9YV290gn> (GitHub repository branch ‘downloader’ available at: <https://github.com/RolnickLab/ClimateSet/tree/downloader>, last accessed 04/2024)  
4, 11, 17, 18
- Kapoor, S., & Narayanan, A. (2023). Leakage and the reproducibility crisis in machine-learning-based science. *Patterns*, 4(9), 100804. Retrieved from <https://doi.org/10.1016/j.patter.2023.100804>  
3
- Kravitz, B., Lynch, C., Hartin, C., & Bond-Lamberty, B. (2017). Exploring precipitation pattern scaling methodologies and robustness among cmip5 models. *Geoscientific Model Development*, 10(5), 1889–1902. Retrieved from <https://doi.org/10.5194/gmd-10-1889-2017>  
16
- Lee, J.-Y., Marotzke, J., Bala, G., Cao, L., Corti, S., Dunne, J., ... Zhou, T. (2021). Future global climate: Scenario-based projections and near-term information. In V. Masson-Delmotte et al. (Eds.), *Climate change 2021: The physical science basis. contribution of working group 1 to the sixth assessment report of the intergovernmental panel on climate change* (pp. 553–672). Cambridge, United Kingdom and New York, NY, USA: Cambridge University Press. Retrieved from <https://doi.org/10.1017/9781009157896.006> (Chapter reference 4.2.4 Pattern Scaling)  
3, 7
- Leith, C. E. (1975). Climate response and fluctuation dissipation. *Journal of Atmospheric Sciences*, 32(10). doi: 10.1175/1520-0469(1975)032<2022:CRAFD>2.0.CO;2  
16
- Leith, C. E. (1978, Nov 01). Predictability of climate. *Nature*, 276(5686), 352-355. Retrieved from <https://doi.org/10.1038/276352a0>  
4, 26
- Lembo, V., Lucarini, V., & Ragone, F. (2020, May 26). Beyond forcing scenarios: Predicting climate change through response operators in a coupled general circulation model. *Scientific Reports*, 10(1), 8668. Retrieved from <https://doi.org/10.1038/s41598-020-65297-2>  
16
- Levy II, H., Horowitz, L. W., Schwarzkopf, M. D., Ming, Y., Golaz, J.-C., Naik, V., & Ramaswamy, V. (2013). The roles of aerosol direct and indirect effects in past and future climate change. *Journal of Geophysical Research: Atmospheres*, 118(10), 4521-4532. Retrieved from <https://doi.org/10.1002/jgrd.50192>  
16

- Lütjens, B. (2023). *Deep learning emulators for accessible climate projections* (PhD thesis, Massachusetts Institute of Technology, Cambridge, MA, USA). Retrieved from <https://hdl.handle.net/1721.1/151644> (Available on MIT DSpace)  
2
- MacDougall, A. H. (2016, Mar 01). The transient response to cumulative co2 emissions: a review. *Current Climate Change Reports*, 2(1), 39-47. Retrieved from <https://doi.org/10.1007/s40641-015-0030-6>  
7, 16
- Maher, N., Lehner, F., & Marotzke, J. (2020, may). Quantifying the role of internal variability in the temperature we expect to observe in the coming decades. *Environmental Research Letters*, 15(5). Retrieved from <https://doi.org/10.1088/1748-9326/ab7d02>  
18
- Maher, N., Milinski, S., & Ludwig, R. (2021). Large ensemble climate model simulations: introduction, overview, and future prospects for utilising multiple types of large ensemble. *Earth System Dynamics*, 12(2), 401-418. Retrieved from <https://doi.org/10.5194/esd-12-401-2021>  
4
- Maher, N., Milinski, S., Suarez-Gutierrez, L., Botzet, M., Dobrynin, M., Kornblueh, L., ... Marotzke, J. (2019). The max planck institute grand ensemble: Enabling the exploration of climate system variability. *Journal of Advances in Modeling Earth Systems*, 11(7), 2050-2069. Retrieved from <https://doi.org/10.1029/2019MS001639>  
9, 26
- Maher, N., Phillips, A. S., Deser, C., Wills, R. C. J., Lehner, F., Fasullo, J., ... Beyerle, U. (2024). The updated multi-model large ensemble archive and the climate variability diagnostics package: New tools for the study of climate variability and change. *EGUsphere*, 2024, 1-28. Retrieved from <https://doi.org/10.5194/egusphere-2024-3684>  
28
- Matthews, J. B. R., Möller, V., van Diemen, R., Fuglestedt, J. S., Masson-Delmotte, V., Méndez, C., ... Reisinger, A. (2021). IPCC AR6 Annex VII: Glossary. In V. Masson-Delmotte et al. (Eds.), *Climate change 2021: The physical science basis. contribution of working group i to the sixth assessment report of the intergovernmental panel on climate change* (pp. 2215-2256). Cambridge, United Kingdom and New York, NY, USA: Cambridge University Press. Retrieved from <https://doi.org/10.1017/9781009157896.022>  
2, 3
- Mauritsen, T., Bader, J., Becker, T., Behrens, J., Bittner, M., Brokopf, R., ... Roeckner, E. (2019). Developments in the mpi-m earth system model version 1.2 (mpi-esm1.2) and its response to increasing co2. *Journal of Advances in Modeling Earth Systems*, 11(4), 998-1038. Retrieved from <https://doi.org/10.1029/2018MS001400>  
7
- Meinshausen, M., Raper, S. C. B., & Wigley, T. M. L. (2011). Emulating coupled atmosphere-ocean and carbon cycle models with a simpler model, magicc6 - part 1: Model description and calibration. *Atmospheric Chemistry and Physics*, 11(4), 1417-1456. Retrieved from <https://doi.org/10.5194/acp-11-1417-2011>  
3, 7
- Mitchell, J. F. B., Johns, T. C., Eagles, M., Ingram, W. J., & Davis, R. A. (1999). Towards the construction of climate change scenarios. *Climatic Change*, 41, 547-581. Retrieved from <https://doi.org/10.1023/A:1005466909820>  
7
- Müller, W. A., Jungclaus, J. H., Mauritsen, T., Baehr, J., Bittner, M., Budich, R., ... Marotzke, J. (2018). A higher-resolution version of the max planck institute earth system model (mpi-esm1.2-hr). *Journal of Advances in Modeling Earth Systems*, 10(7), 1383-1413. Retrieved from <https://doi.org/10.1029/2017MS001217>  
2

- Nguyen, T., Brandstetter, J., Kapoor, A., Gupta, J. K., & Grover, A. (2023, 23–29 Jul). ClimaX: A foundation model for weather and climate. *Proceedings of the 40th International Conference on Machine Learning, 202*, 25904–25938. Retrieved from <https://proceedings.mlr.press/v202/nguyen23a.html>  
4, 11, 12, 29
- O’Gorman, P. A., Allan, R. P., Byrne, M. P., & Previdi, M. (2012, Jul 01). Energetic constraints on precipitation under climate change. *Surveys in Geophysics*, *33*(3), 585–608. Retrieved from <https://doi.org/10.1007/s10712-011-9159-6>  
32, 33
- Olonscheck, D., Suarez-Gutierrez, L., Milinski, S., Beobide-Arsuaga, G., Baehr, J., Fröb, F., ... Brune, S. (2023). The new max planck institute grand ensemble with cmip6 forcing and high-frequency model output. *Journal of Advances in Modeling Earth Systems*, *15*(10), e2023MS003790. Retrieved from <https://doi.org/10.1029/2023MS003790>  
4, 7, 9
- O’Neill, B. C., Tebaldi, C., van Vuuren, D. P., Eyring, V., Friedlingstein, P., Hurtt, G., ... Sanderson, B. M. (2016). The scenario model intercomparison project (scenariomip) for cmip6. *Geoscientific Model Development*, *9*(9), 3461–3482. Retrieved from <https://doi.org/10.5194/gmd-9-3461-2016>  
5
- Pedregosa, F., Varoquaux, G., Gramfort, A., Michel, V., Thirion, B., Grisel, O., ... Duchesnay, E. (2011). Scikit-learn: Machine learning in Python. *Journal of Machine Learning Research*, *12*, 2825–2830. Retrieved from <http://jmlr.org/papers/v12/pedregosa11a.html>  
8
- Richters, O., Kriegler, E., Bertram, C., Cui, R., Edmonds, J., Fawcett, A., ... Zhao, X. (2024, November). *Ngfs climate scenarios technical documentation v5.0* [Technical Documentation].  
2
- Santer, B. D., Wigley, T. M. L., Schlesinger, M. E., & Mitchell, J. F. B. (1990). Developing climate scenarios from equilibrium gcm results. *Report / Max-Planck-Institut für Meteorologie*, *047*, 29. Retrieved from <https://hdl.handle.net/21.11116/0000-0001-68B8-B>  
3
- Sarofim, M. C., Smith, J. B., St. Juliana, A., & Hartin, C. (2021, Jan). Improving reduced complexity model assessment and usability. *Nature Climate Change*, *11*(1), 1-3. Retrieved from <https://doi.org/10.1038/s41558-020-00973-9>  
3
- Seland, Ø., Bentsen, M., Olivié, D., Toniazzo, T., Gjermundsen, A., Graff, L. S., ... Schulz, M. (2020). Overview of the norwegian earth system model (noresm2) and key climate response of cmip6 deck, historical, and scenario simulations. *Geoscientific Model Development*, *13*(12), 6165–6200. Retrieved from <https://doi.org/10.5194/gmd-13-6165-2020>  
5
- Sherwood, S. C., Webb, M. J., Annan, J. D., Armour, K. C., Forster, P. M., Hargreaves, J. C., ... Zelinka, M. D. (2020). An assessment of earth’s climate sensitivity using multiple lines of evidence. *Reviews of Geophysics*, *58*(4), e2019RG000678. Retrieved from <https://doi.org/10.1029/2019RG000678>  
27
- Shi, X., Chen, Z., Wang, H., Yeung, D.-Y., Wong, W.-k., & Woo, W.-c. (2015). Convolutional lstm network: A machine learning approach for precipitation nowcasting. In *Advances in neural information processing systems* (Vol. 28). Curran Associates, Inc. Retrieved from [https://papers.nips.cc/paper\\_files/paper/2015/hash/07563a3fe3bbe7e3ba84431ad9d055af-Abstract.html](https://papers.nips.cc/paper_files/paper/2015/hash/07563a3fe3bbe7e3ba84431ad9d055af-Abstract.html)  
8

- Sippel, S., Meinshausen, N., Merrifield, A., Lehner, F., Pendergrass, A. G., Fischer, E., & Knutti, R. (2019). Uncovering the forced climate response from a single ensemble member using statistical learning. *Journal of Climate*, *32*(17), 5677 - 5699. Retrieved from <https://doi.org/10.1175/JCLI-D-18-0882.1>  
18
- Smith, C. (2021). *Guest post: The role ‘emulator’ models play in climate change projections*. Retrieved from <https://www.carbonbrief.org/guest-post-the-role-emulator-models-play-in-climate-change-projections/> (last accessed 05/2024)  
3
- Smith, C. J., Forster, P. M., Allen, M., Leach, N., Millar, R. J., Passerello, G. A., & Regayre, L. A. (2018). Fair v1.3: a simple emissions-based impulse response and carbon cycle model. *Geoscientific Model Development*, *11*(6), 2273–2297. Retrieved from <https://doi.org/10.5194/gmd-11-2273-2018>  
7
- Smith, C. J., Harris, G. R., Palmer, M. D., Bellouin, N., Collins, W., Myhre, G., ... Forster, P. M. (2021). Energy budget constraints on the time history of aerosol forcing and climate sensitivity. *Journal of Geophysical Research: Atmospheres*, *126*(13). Retrieved from <https://doi.org/10.1029/2020JD033622>  
26
- Swaminathan, R., Schewe, J., Walton, J., Zimmermann, K., Jones, C., Betts, R. A., ... Weigel, K. (2024). Regional impacts poorly constrained by climate sensitivity. *Earth’s Future*, *12*(12).  
27
- Tang, Y., Zhang, R.-H., Liu, T., Duan, W., Yang, D., Zheng, F., ... Mu, M. (2018, 10). Progress in ENSO prediction and predictability study. *National Science Review*, *5*(6), 826-839. Retrieved from <https://doi.org/10.1093/nsr/nwy105>  
26
- Tebaldi, C., & Arblaster, J. M. (2014, Feb 01). Pattern scaling: Its strengths and limitations, and an update on the latest model simulations. *Climatic Change*, *122*(3), 459-471. Retrieved from <https://doi.org/10.1007/s10584-013-1032-9>  
3, 8, 16
- Tebaldi, C., Armbruster, A., Engler, H. P., & Link, R. (2020). Emulating climate extreme indices. *Environmental Research Letters*, *15*(7). Retrieved from <https://doi.org/10.1088/1748-9326/ab8332>  
16
- Tebaldi, C., Dorheim, K., Wehner, M., & Leung, R. (2021). Extreme metrics from large ensembles: investigating the effects of ensemble size on their estimates. *Earth System Dynamics*, *12*(4), 1427–1501. Retrieved from <https://doi.org/10.5194/esd-12-1427-2021>  
4, 9, 13, 14
- Tebaldi, C., Selin, N., Ferrari, R., & Flierl, G. (2025). *Emulators of climate model output*. (in press)  
3
- Tokarska, K. B., Stolpe, M. B., Sippel, S., Fischer, E. M., Smith, C. J., Lehner, F., & Knutti, R. (2020). Past warming trend constrains future warming in cmip6 models. *Science Advances*, *6*(12), eaaz9549. Retrieved from <https://doi.org/10.1126/sciadv.aaz9549>  
27
- Wang, C., Pritchard, M. S., Brenowitz, N., Cohen, Y., Bonev, B., Kurth, T., ... Pathak, J. (2024). *Coupled ocean-atmosphere dynamics in a machine learning earth system model*. Retrieved from <https://arxiv.org/abs/2406.08632>  
3
- Watson-Parris, D. (2022, September). *Climatebench*. Zenodo. Retrieved from <https://doi.org/10.5281/zenodo.7064308> (version 1.0.0)

18

- Watson-Parris, D., Rao, Y., Olivié, D., Seland, O., Nowack, P., Camps-Valls, G., . . . Roesch, C. (2022). Climatebench v1.0: A benchmark for data-driven climate projections. *Journal of Advances in Modeling Earth Systems*, *14*(10), e2021MS002954. Retrieved from <https://doi.org/10.1029/2021MS002954>  
3, 4, 8, 11, 12, 26, 28, 29, 30, 33
- Watt-Meyer, O., Dresdner, G., McGibbon, J., Clark, S. K., Henn, B., Duncan, J., . . . Bretherton, C. S. (2023). *Ace: A fast, skillful learned global atmospheric model for climate prediction*. Retrieved from <https://doi.org/10.48550/arXiv.2310.02074>  
3
- Wells, C. D., Jackson, L. S., Maycock, A. C., & Forster, P. M. (2023). Understanding pattern scaling errors across a range of emissions pathways. *Earth System Dynamics*, *14*(4), 817–834. Retrieved from <https://doi.org/10.5194/esd-14-817-2023>  
8, 11, 16
- Wieners, K.-H., Giorgetta, M., Jungclaus, J., Reick, C., Esch, M., Bittner, M., . . . Roeckner, E. (2019). *Mpi-m mpiesm1.2-lr model output prepared for cmip6 cmip*. Earth System Grid Federation. Retrieved from <https://doi.org/10.22033/ESGF/CMIP6.742>  
18
- Williams, A. I. L., Stier, P., Dagan, G., & Watson-Parris, D. (2022, Aug). Strong control of effective radiative forcing by the spatial pattern of absorbing aerosol. *Nature Climate Change*, *12*(8), 735–742. Retrieved from <https://doi.org/10.1038/s41558-022-01415-4>  
-4  
16
- Williams, A. I. L., Watson-Parris, D., Dagan, G., & Stier, P. (2023). Dependence of fast changes in global and local precipitation on the geographical location of absorbing aerosol. *Journal of Climate*, *36*(18), 6163 - 6176. Retrieved from <https://doi.org/10.1175/JCLI-D-23-0022.1>  
16
- Wills, R. C. J., Battisti, D. S., Armour, K. C., Schneider, T., & Deser, C. (2020). Pattern recognition methods to separate forced responses from internal variability in climate model ensembles and observations. *Journal of Climate*, *33*(20), 8693 - 8719. Retrieved from <https://doi.org/10.1175/JCLI-D-19-0855.1>  
18
- Womack, C. B., Giani, P., Eastham, S. D., & Selin, N. E. (2025). Rapid emulation of spatially resolved temperature response to effective radiative forcing. *Journal of Advances in Modeling Earth Systems*, *17*(1). doi: <https://doi.org/10.1029/2024MS004523>  
16

## Appendix A Definitions

### A1 Background on internal variability

Internal variability refers to natural fluctuations in weather and climate (Leith, 1978). These fluctuations are often decomposed into modes with periods of varying lengths, such as the Madden-Julian Oscillation (1-3 months), El Niño Southern Oscillation (2-7 years), or Atlantic Multidecadal Oscillation (60-70 years). The magnitude of the associated amplitudes can be at the same scale or higher than the emission-induced climate change, depending on the climate variable of interest. It is known that the exact transition times of some of those climate modes, such as ENSO, are unpredictable on climate timescales (Tang et al., 2018). Thus, climate scientists often treat the fluctuations as “climate noise” and identify the forced signal by taking an ensemble average over a sufficiently large set of climate simulations (Maher et al., 2019). These ensembles can be called single model initial-condition ensembles (SMILEs) and contain multiple realizations, i.e., simulations, runs, or members, of a single model that is forced by the same emission pathway but with slightly different initial conditions on every run.

## Appendix B Extended Data & Methods

### B1 Appendix to Background on ClimateBench dataset, evaluation protocol, and metrics

#### *B11 Definition of variables in ClimateBench inputs and targets*

The variables are defined as:

- $\text{CO}_{2,t}$  are the carbon dioxide emissions, from anthropogenic sources, summed over the globe and the year,  $t$ . The cumulative carbon dioxide emissions,  $\text{CO}_{2,t}^{cum}$ , are summed from 1850 until the end of the target year,  $t$ . We visualize the data in gigatons of carbon dioxide, GtCO<sub>2</sub>, (one gigaton is one billion tons) in Fig. B1.
- $\text{CH}_{4,t}$  are the anthropogenic methane emissions summed over the globe and year,  $t$ .
- $\text{SO}_{2,i,j,t}$  are the anthropogenic sulfur-dioxide emissions summed over the area of grid cell  $(i, j)$  and year,  $t$ . Figure B1 shows that the emission pathways for SO<sub>2</sub> contain a discontinuity between historical and ssp scenarios at year 2014-15. This discontinuity exists in the official CMIP6 data and has been updated in the 2022 CEDS data, as illustrated in (C. J. Smith et al., 2021)-Fig. S2, but the NorESM2-LM and Em-MPI targets were still generated with the official CMIP6 forcings.
- $\text{BC}_{i,j,t}$  are the anthropogenic black carbon emissions summed over the area of grid point  $(i, j)$  and year,  $t$ .
- $\text{tas}_{i,j,t}$  are the annual mean surface temperature anomalies at 2m height. The surface temperature anomaly is the surface temperature minus the average surface temperature of the preindustrial control simulation at each grid point. The unit is deg  $C$ . The globally-averaged values are plotted in Fig. B2.
- $\text{dtr}_{i,j,t}$  is the annual mean diurnal temperature range anomaly wrt. the preindustrial control run in deg  $C$ . The diurnal temperature range was calculated by first subtracting the minimum from the maximum daily temperature and then averaging over the year.
- $\text{pr}_{i,j,t}$  is the annual mean total precipitation per day in  $mm/day$ . The value is reported as anomaly wrt. to the preindustrial control run.
- $\text{pr90}_{i,j,t}$  is the 90th percentile of the daily precipitation in each year.
- We refer to Watson-Parris et al. (2022) for more details.

To analyze the linearity we have plotted the correlation between temperature and global CO<sub>2</sub> in Fig. B2.

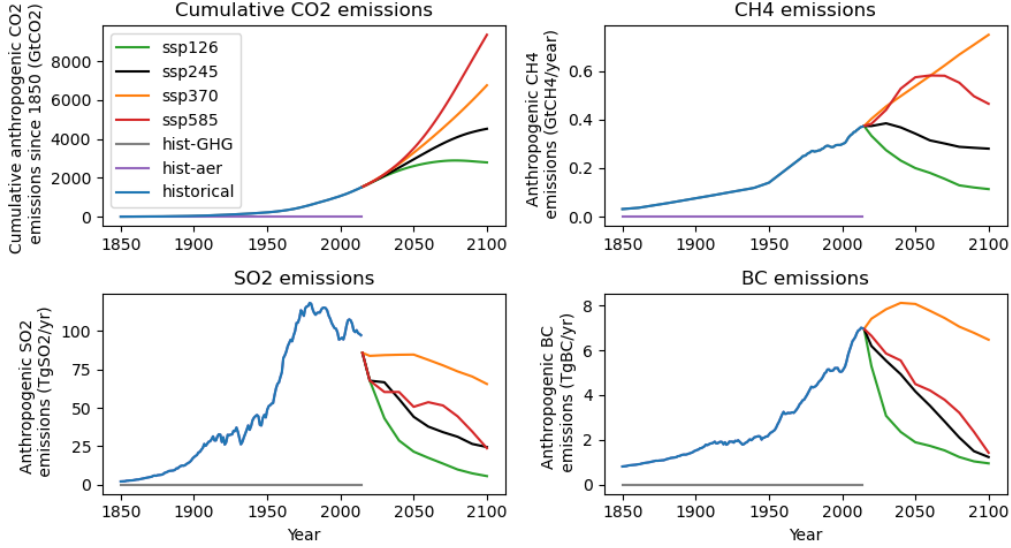


Figure B1: **Emission pathways over time.** The plots show multiple emission pathways for each forcing variable. The  $\text{CO}_2$  emissions (top-left) are plotted as sums over the globe and years since 1850. The methane (top-right), sulfur-dioxide (bottom-left), and black carbon (bottom-right) are plotted as global sums per year.  $\text{SO}_2$  contains a discontinuity between historical and ssp scenarios. The ClimateBench inputs contain global values for  $\text{CO}_2^{\text{cum}}$  and  $\text{CH}_4$  and locally-resolved values for  $\text{SO}_2$  and  $\text{BC}$  (not shown).

### B12 Evaluation metrics in ClimateBench

For the results table in ClimateBench (see Table 1), the RMSE is normalized by the magnitude of the target variable to compute the NRMSEs, where we denote the placeholder  $* \in \{s, g\}$ :

$$\text{NRMSE}_*(\hat{\mathbf{Y}}_e, \mathbf{Y}_e) = \frac{\text{RMSE}_*}{\left| \frac{1}{\sum_i \alpha_{i,j}} \sum_{i,j} \alpha_i \frac{1}{|\mathbb{T}_{\text{test}}|} \sum_t \frac{1}{|\mathbb{M}|} \sum_m y_{i,j,t,m,e} \right|_{\text{abs}}} \quad (\text{B1})$$

The ClimateBench evaluation protocol and results table also contain the weighted sum of  $5 \times$  global + spatial NRMSE, called “total” NRMSE. The total NRMSE was proposed in the ClimateBench paper as a metric on which the “best” emulator can be declared and the factor of 5 was chosen to equalize the scales between both errors.

The ClimateBench evaluation metrics in Eqs. (1), (2) and (B1) are consistent with the ClimateBench paper Sect. 3.1. Eq. (1-3) except for a slightly different notation.

## B2 Appendix to Em-MPI data

We followed the Hausfather et al. (2022) recommendation to avoid using “hot” models and decided against using CanESM5 with the transient climate response,  $\text{TCR} \approx 2.7^\circ$ , being outside the  $[1.4, 2.2]^\circ\text{C}$  likely range and the equilibrium climate sensitivity,  $\text{ECS} \approx 5.6^\circ\text{C}$ , being outside the  $[2.3, 4.7]^\circ\text{C}$  very likely range (Tokarska et al., 2020; Sherwood et al., 2020). However, excluding hot models from climate analyses is an ongoing point of discussion, especially for regional climate analysis (Swaminathan et al., 2024), and CanESM5 might provide a valuable reference for future benchmarking of emulators. We decided against using EC-Earth3 because many realizations were unavailable on the Earth System Grid

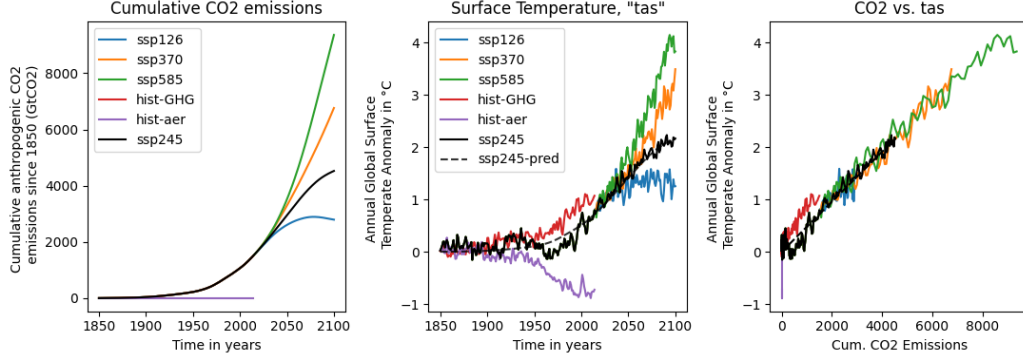


Figure B2: **Correlation between temperature and global  $\text{CO}_2^{\text{cum}}$  with 3-member NorESM2-LM targets.** The left plot shows the input cumulative  $\text{CO}_2$  emissions over time for each training scenario (ssp126, -370, -585, hist-GHG, hist-aer) and test scenario (ssp245), averaged over three realizations of the NorESM2-LM model. The middle plot shows the annual globally-averaged surface temperature anomalies, wrt. the preindustrial control, over time for each scenario. The black-dotted line indicates the linear pattern scaling emulator prediction. On the right, we plot the data against each other. We can see that global temperature and  $\text{CO}_2^{\text{cum}}$  are linearly correlated except for the high-frequency variations, the hist-aer scenario that ablates  $\text{CO}_2^{\text{cum}}$ , and a dip in 1970-2000.

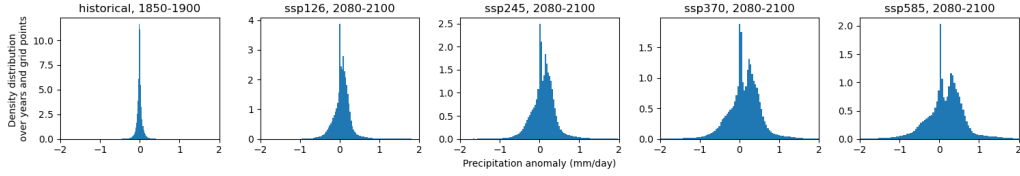
Federation (ESGF) Portal, but they may be retrievable through other pathways. For MPI-ESM1.2-LR all realizations were either already available or rapidly made available on ESGF after inquiry with the data owners. The MMLEAv2 was unavailable at the start of this work, but contains 30+ realizations of the Tier 1 SSPs for a few additional ESMs (Maher et al., 2024).

The precipitation targets in the Em-MPI dataset do not follow a log-normal distribution as visualized in Fig. B3. Instead, Fig. B3a shows that the spatial distribution of annually- and ensemble-averaged precipitation anomalies follow a bimodal distribution that contains negative values. The mode at zero indicates locations with no projected precipitation change. With increasing  $\text{CO}_2^{\text{cum}}$  from historical over ssp126 to ssp585, the distribution’s second mode increases and the overall distribution broadens towards heavier tails. Figure B3b shows the ensemble distributions of annually-averaged precipitation anomalies over a subset of the historical period for multiple randomly picked locations within IPCC AR6 regions. Some distributions appear to have the shape of log-normal distributions, but all distributions contain negative values.

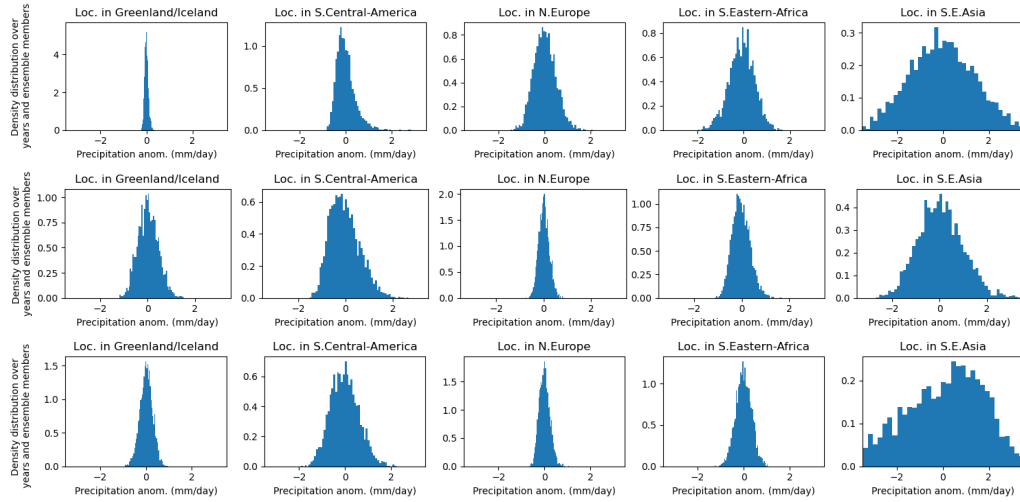
### B3 Details of the CNN-LSTM-based emulator

The CNN-LSTM in the ClimateBench results table (Watson-Parris et al., 2022) uses the spatial input fields of  $\text{CO}_2$ ,  $\text{CH}_4$ , BC, and  $\text{SO}_2$  over a 10-year time window as input, resulting in the input shape:  $(4, I, J, h_t)$  with the time history length  $h_t = 10$  years. The input grid size,  $(I = 96, J = 144)$ , is independent of which targets are being predicted. As  $\text{CO}_2$  and  $\text{CH}_4$  are global variables, their input fields are filled with a single scalar value that is repeated along the  $I, J$  dimensions.

The emulator predicts the spatial field for the target year at the end of the time history with the output shape  $(1, I, J, 1)$  with  $(I, J) = (96, 144)$  or  $(I^{\text{em-mpi}}, J^{\text{em-mpi}}) = (96, 192)$  for the NorESM2-LM or Em-MPI targets, respectively. For each target climate variable, a different CNN-LSTM is trained independently. The input variables are normalized to zero-mean, unit-variance; the target variables are not normalized, following (Watson-Parris et



(a) Spatial distributions of precipitation anomalies. Each histogram shows the distribution of annually- and ensemble-averaged precipitation anomalies over all grid points and years in the selected timeframe for a given scenario. We select short time frames – 1850-1900 for historical and 2080-2100 for the ssp-scenarios – to increase the sample size but maintain minimal influence from changing emissions.



(b) Ensemble distributions of precipitation anomalies. Each histogram shows the distribution of annually-averaged precipitation anomalies over all 50 members in the ensemble, and years in a subset of the historical period (1850-1900). Each column shows the distributions for a different region, and each row shows a different randomly selected grid cell within this region.

**Figure B3: Distributions of precipitation anomalies in the Em-MPI dataset.** The y-axis value is the count in each bin, divided by the total number of counts and bin width, such that the density integrates to one. The x-axis is scaled to fixed values to allow for comparison between subplots.

al., 2022). The values for the CNN-LSTM (reproduced) are originally reported in (Nguyen et al., 2023).

We reimplement the same CNN-LSTM as in (Watson-Parris et al., 2022) for our internal variability experiment. The model architecture is akin to an autoencoder-LSTM-decoder structure, because the LSTM does not maintain any spatial dimensions and there are no skip connections from en- to decoder. The emulator first applies the same convolutional layer with 20 filters of size (3, 3) to every year in the input window independently. Then, the spatial dimension is reduced to 1 with a 2x2 average pooling layer and a consecutive global average pooling layer. The latent time-series with 20 feature and 1 spatial dimension(s) is fed into an LSTM layer with 25 output features and ReLU activation. Finally, a dense layer projects the features of shape (25,  $h_t$ ) onto the output shape. Most learnable weights (~ 95%) are in this final dense output layer.

The CNN-LSTM is optimized with an objective function that minimizes the pixel- and year-wise MSE:

$$\mathbb{E}_{t,e \sim \mathbb{D}_{t,e}} \left[ \frac{1}{IJ} \sum_{ij} (\hat{y}_{i,j,t,e} - \frac{1}{|\mathbb{M}|} \sum_m y_{i,j,t,m,e})^2 \right] \quad (\text{B2})$$

where  $\mathbb{D}_{t,e} = \mathbb{T}_{train} \cup \mathbb{S}_{e,train}$  is the set of all years,  $\mathbb{T}_{train} = \{1850, 1851, \dots, 2100\}$ , and scenarios,  $\mathbb{S}_{e,train}$ , used during training. The optimizer is RMSprop with the learning rate 0.001, no weight decay, and batch size 16. These hyperparameter choices are the same as in (Watson-Parris et al., 2022). We implemented the emulator using keras 3.0 with a pytorch backend, differing from the keras 2.0+tensorflow backend in (Watson-Parris et al., 2022). On the Em-MPI targets dataset, the emulator has more parameters than on the ClimateBench targets dataset due to the higher resolution target grid (see Tables 1 and 2 for the exact number).

It is likely possible to improve the scores of this CNN-LSTM. For example, the variance over weight initialization random seeds indicates suboptimal optimization parameters. A possible solution would be to create a separate validation set by withholding samples from the training set, and to use the validation set for tuning optimization parameters, such as learning rate and weight decay. But, the aim of this paper is not to develop a high-scoring emulation technique and, instead, to discuss the influence of internal variability onto benchmarking scores. To make a fair comparison of the role played by internal variability in the NorESM data in ClimateBench by using the Em-MPI data, we decided to follow ClimateBench’s implementation of this CNN-LSTM as exactly as possible. Given that the CNN-LSTM implementation in ClimateBench does not use a validation set and does not optimize the hyperparameters, we also chose not to do so. To report statistically reliable statistics despite the variance in random weight initialization seed, we deviate from the original implementation by averaging over multiple training runs.

#### B4 Appendix to Testing the influence of internal variability

The mean RMSE in the internal variability experiment for the CNN-LSTM with random weight initialization seed,  $l$ , is calculated as:

$$\text{RMSE}_{*,n}^{exp} = \frac{1}{K} \sum_{k \in \{1, \dots, K\}} \frac{1}{L} \sum_{l \in \{1, \dots, L\}} \text{RMSE}_* \left( \hat{f}_{n,k,l}(\mathbf{X}_{test}), \mathbb{E}_{\mathbb{M}}[\mathbf{Y}_{test}] \right) \quad (\text{B3})$$

### Appendix C Extended Results & Discussion

#### C1 Appendix to Evaluation of Linear Pattern Scaling on ClimateBench

For completeness, we repeat the linear pattern scaling error map for diurnal temperature range, precipitation, and 90th percentile precipitation in Figs. C1 to C3, respectively. Equivalent plots for the Gaussian Process, Neural Network, and Random Forest emulators can be found in (Watson-Parris et al., 2022)-Fig. 4.

#### C2 Appendix to Magnitude of internal variability in 3-member NorESM2-LM and 50-member MPI-ESM1.2-LR ensemble average

Figure C4 shows the internal variability in the 3-member ensemble mean of the NorESM2-LM (used in ClimateBench) and 50-member Em-MPI data for multiple regions. The regions were selected to illustrate the local variation in the dataset.

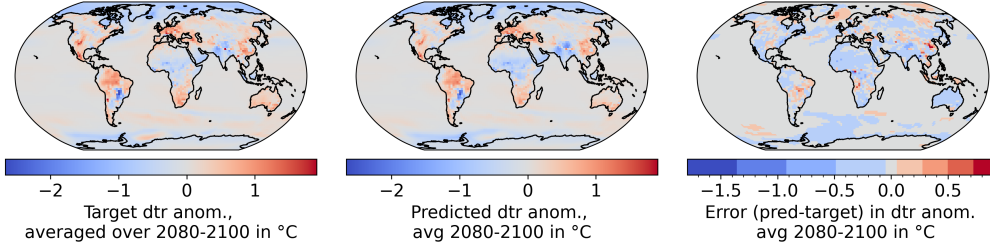


Figure C1: **Linear pattern scaling error map for diurnal temperature range.** The left column shows the target anomalies from the ssp245 ClimateBench test set, averaged over 3 realizations and 21 years (2080-2100). The middle plot shows the linear pattern scaling predictions and the right plot the error of predictions minus the target.

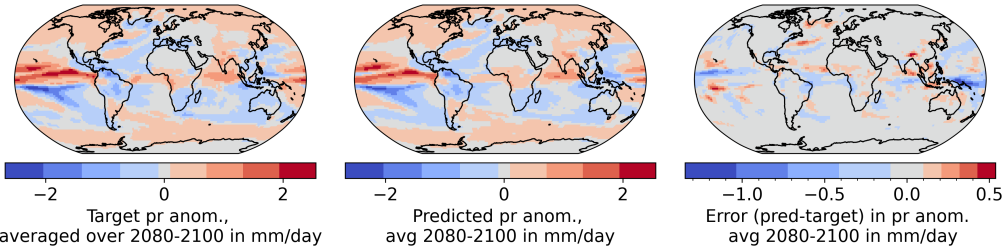


Figure C2: **Linear pattern scaling error map, similar to Fig. C1, for precipitation.**

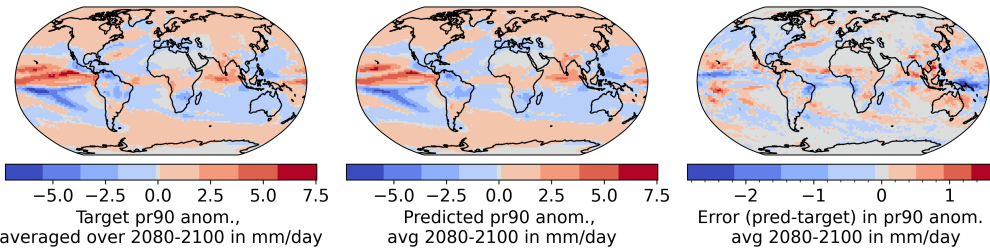


Figure C3: **Linear pattern scaling error map, similar to Fig. C1, for 90th percentile precipitation.**

### C3 Appendix to Effect of internal variability on benchmarking scores

Figure C5 shows the trend of the difference in spatial RMSE,  $\Delta RMSE_{*,s}(n)$  for spatial precipitation and surface temperature over an increasing number of realizations in the train set. Both climate variables show a downward trend over the x-axis inset from [0,20].

### C4 Functional relationships of Em-MPI temperature and precipitation for multiple regions

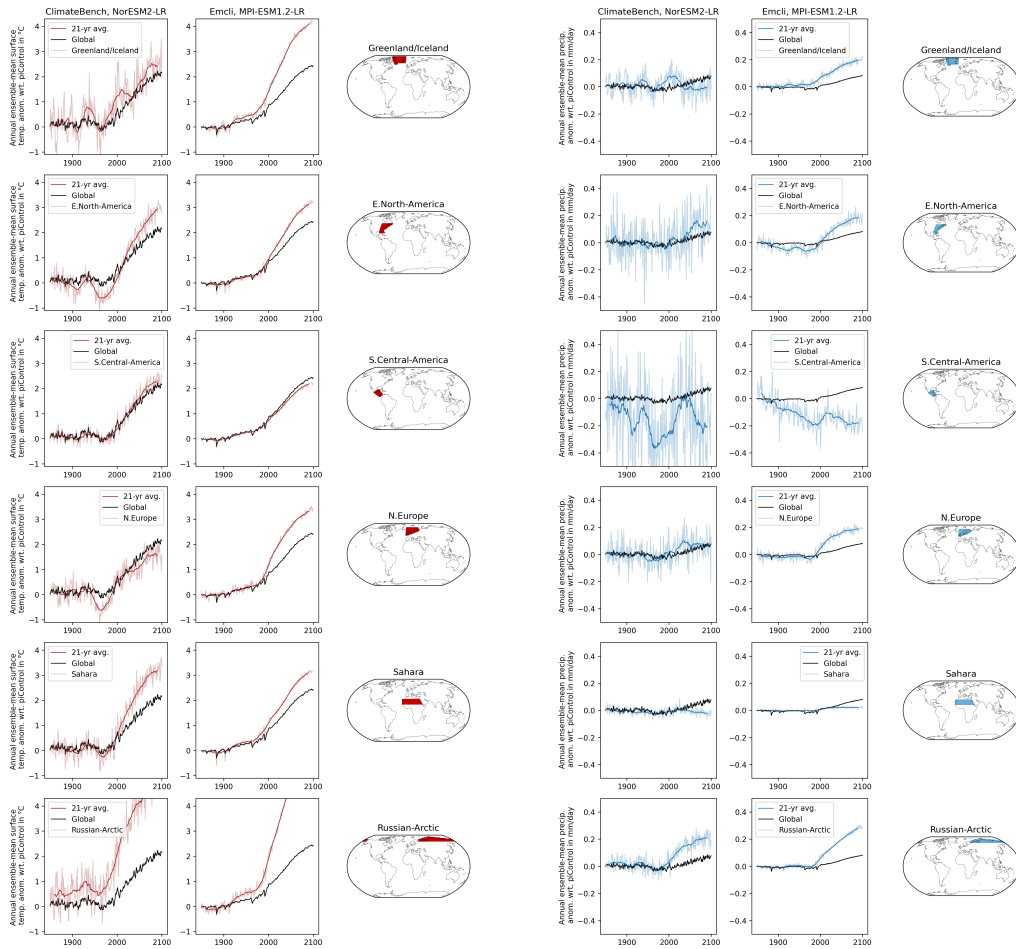
To understand the relationships between cumulative CO<sub>2</sub> emissions, surface temperature, and precipitation further, we plot the regionally-averaged values for the Em-MPI data in Fig. C6. We selected five regions from the IPCC AR6 regions to illustrate that there are linear and nonlinear relationships depending on the location. We selected S.Eastern-Africa to highlight the nonlinear relationships in temperature and S.E.Asia for precipitation. The scatter in the precipitation plots suggests that the variable depends on more variables than

global cumulative CO<sub>2</sub> emissions, which goes in line with aerosols possibly influencing the precipitation in this area.

### C5 Discussion of regional error distribution, global precipitation, and diurnal temperature range scores on ClimateBench

The distribution of linear pattern scaling errors in Fig. 4 (right) shows that LPS overpredicts warming in the North Atlantic “cold blob”, Weddell Sea, and Northern Asia. The emulator underpredicts warming in the Norwegian Sea and along the South Atlantic Current. The error in Northern Asia might be due to the missing aerosol inputs. The error in the Weddell and Norwegian Sea could be due to the nonlinearities from changing sea ice extent. LPS also shows sporadically located errors of small spatial extent but noteworthy magnitude, e.g., in Central Africa or South East Asia, which could be due to internal variability in the target climate model data.

For precipitation and 90th percentile precipitation in Table 1, linear pattern scaling has lower spatial NRMSE while ClimaX has lower global NRMSE. This possibly relates to the varying timescales in the precipitation response: If CO<sub>2</sub> is rapidly increased and temperature has not yet increased, global-mean precipitation decreases due to radiative cooling; only after temperatures have increased the global-mean precipitation settles to zero again (O’Gorman



(a) Surface Temperature  
(continued on next page)

(b) Precipitation  
(continued on next page)

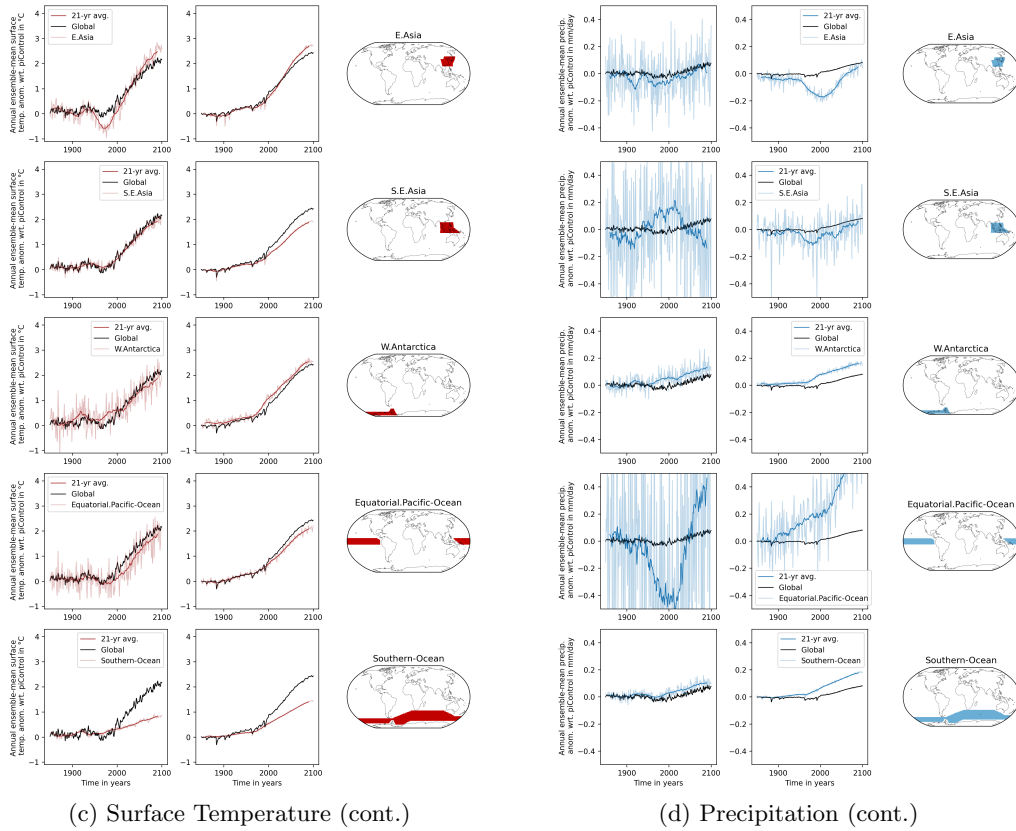


Figure C4: Ensemble-mean of surface temperature (a, c) and precipitation (b,d) of 3-member NorESM2-LM (left sub-columns) vs. 50-member MPI-ESM1.2-LR data (middle sub-columns) for the ssp245 scenario and selected regions (right sub-columns) representing distinct distributions. The regional averages are further averaged over each year (shaded) or 21-year window (opaque). PDF reader with zoom required.

et al., 2012). Whereas, local precipitation is more related to horizontal moisture transport which scales with local temperatures that increase with long-term  $\text{CO}_2^{cum}$  rise (O’Gorman et al., 2012). However, this discrepancy in the ClimateBench scores could also be an artifact of the internal variability influence. ClimaX has the lowest scores for diurnal temperature range, which could be due to the strong correlation with aerosols (Watson-Parris et al., 2022).

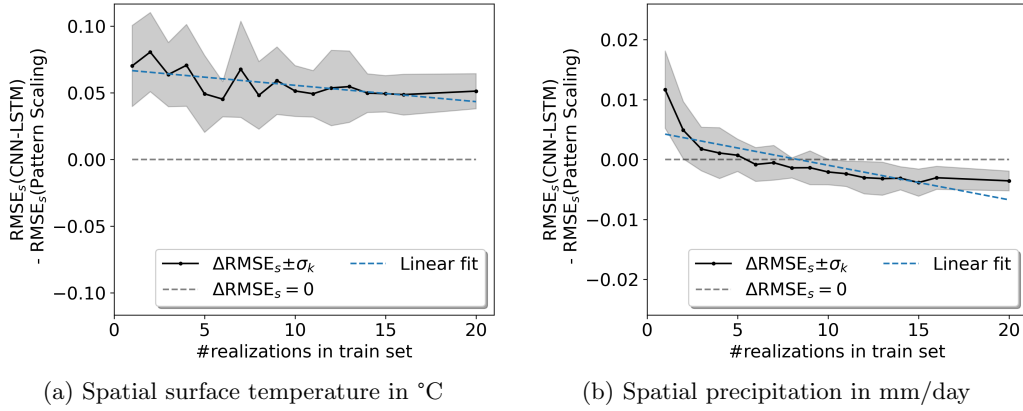


Figure C5: **Linear trend of  $\Delta RMSE_{*,s}(n)$  over an x-axis inset.** The plots show  $\Delta RMSE$  for spatial surface temperature (left) and spatial precipitation (right) for an x-axis inset from  $[0, 20]$  and the best linear fit (blue) over the values in this inset. We choose a linear x-scale (instead of the log-scale in Fig. 5) to illustrate the negative linear slope.

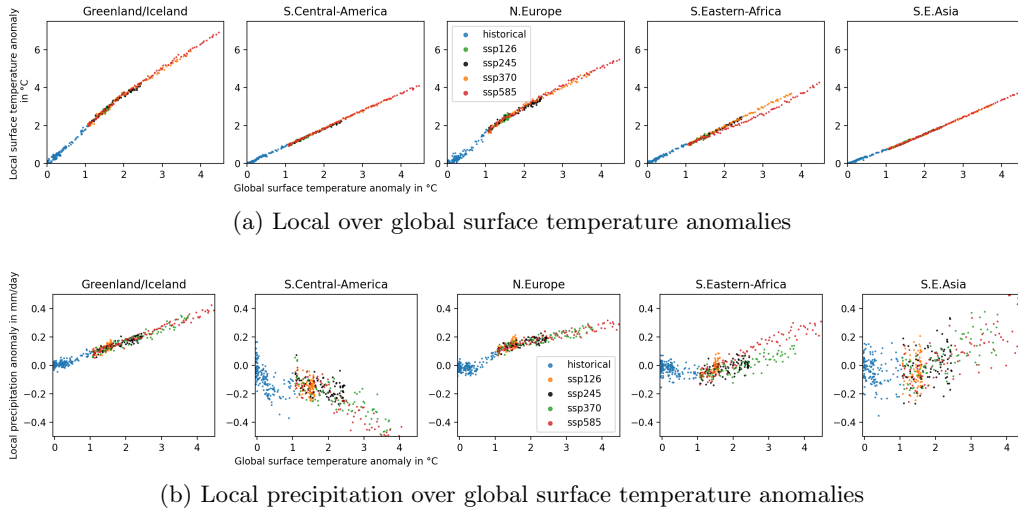


Figure C6: **Functional relationships for multiple regions.** The top row plots regionally-averaged over globally-averaged surface temperature anomalies for multiple IPCC AR6 regions. Similarly, the bottom rows plots the regionally-averaged precipitation anomalies over global surface temperature anomalies.

## Appendix D Bias-variance experiment

### D1 Experiment set-up

In this pedagogical model, the target variable is a hypothetical climate variable anomaly,  $y_t$ , that is comparable to precipitation and relates nonlinearly to the temperature anomaly,  $T_t$ , via  $y_t = g(T_t)$ . Both variables are local, i.e., they represent the state of a generic atmosphere-ocean column. The change of the column's temperature anomaly,  $dT_t$ , is simulated via a local energy balance model, similar to (Eq. 6) in Giani et al. (2024).

$$dT_t = \frac{r}{C}X_t dt + \frac{\lambda}{C}T_t dt + \sigma dW_t \quad (\text{D1})$$

The first term on the right-hand (rhs) side represents the radiative forcing expressed as a linear function of cumulative emissions of a hypothetical greenhouse gas,  $X_t$ . (In analogy to carbon dioxide, the radiative forcing is assumed to be proportional to the greenhouse gas concentration, which in turn is proportional to cumulative emissions for long-lived gases.)  $C$  is the effective heat capacity of the atmosphere-ocean column, and  $r$  is the local perturbation radiative forcing per unit of cumulative greenhouse gas emissions. The second rhs term represents climate feedbacks that act to bring the temperature back to equilibrium and  $\lambda$  is a negative feedback parameter. The last rhs term is a noise term, not standard in the energy balance model, here included representing the internal variability generated by nonlinear processes and transport terms Hasselmann (1976). The noise is sampled from a zero mean Gaussian distribution with variance  $dt$  independently at each time step,  $dW_t \sim \mathcal{N}(0, dt; \omega)$ .  $\sigma$  sets the amplitude of the internal variability and  $\omega$  sets the random seed.

We simulate equation (D1) by choosing a curve of cumulative emissions that looks similar to ssp245,  $X_t = X_p \exp(-(t - t_p)^2 / 2\sigma_X)$ , with the peak cumulative emissions,  $X_p = 5000 \text{GtX}$ , the timing of the peak,  $t_p = 250 \text{yr}$ , and the shape parameter,  $\sigma_X = 50 \text{yr}$ . We choose  $r = 0.0008 \text{Wm}^{-2} \text{GtX}^{-1}$ . The column heat capacity is given by,  $C = \rho_w c_w h$ , with the density of water,  $\rho_w = 997 \text{kgm}^{-3}$ , the specific heat capacity of water,  $c_w = 4184 \text{Wskg}^{-1} \text{K}^{-1}$ , and the effective column-integrated water depth,  $h$ . We choose the values for a low-latitude ocean column in Giani et al. (2024):  $h = 150 \text{m}$ ,  $\lambda = -2 \text{Wm}^{-2} \text{K}^{-1}$ . We solve the equation via explicit integration in time, i.e.,  $T_t = T_{t-1} + dT_t dt$ , with  $T_0 = 0 \text{K}$ ,  $dt = 1 \text{yr}$ ,  $t_0 = 0 \text{yr}$ , and  $t_{\max} = 250 \text{yr}$ . Lastly, we chose  $g$  as an arbitrary quadratic function  $g(T_t) = 0.03(4T_t)^2$ .

Analogously to the ensemble averages in the internal variability experiment, we construct many training sets with differing number of realizations from this function. Each  $n$ -member training set is given by  $\mathbf{Y}_{n,k} = \{y_{t,n,k} | t \in \mathbb{T}\}$  with  $\mathbb{T} = \{t_0, \dots, t_{\max} - 1\}$  and:

$$y_{t,n,k} = \frac{1}{n} \sum_{m \in \{1, \dots, n\}} y_t(\omega_{m,n,k}) \quad (\text{D2})$$

where  $n$  denotes the number of realizations in a training set,  $k$  denotes the  $k$ th random draw of equally-sized ensembles, and  $\omega_{m,n,k}$  denotes the random seed for every  $m - n - k$  combination. Different from the internal variability experiment, we assume an infinite set of realizations, i.e.,  $\omega_{m,n,k}$  is drawn with replacement, s.t., statistics are also reliable for large  $n$ .

Each neural network and linear model is fitted using a scalar,  $X_t$ , as input and output the scalar,  $\hat{y}_{t,n,k}$ . For each  $n-k$  combination, the training set consists of 250 ( $t_{\max}$ ) datapoints of the function sample,  $y_{t,n,k}$ . For each training set, we draw a new validation set as another sample of the function,  $y_{t,n,k}$ , with the same  $n$ . The test set, for which the MSE and Bias<sup>2</sup> are reported, is the noise-free emission-forced signal,  $\bar{y}_t$ , given by integrating Eq. (D1) while omitting the  $\sigma dW_t$  term. The expected scores are computed with  $K = 2000$ .

We choose a fully-connected neural network that has two hidden layers of 64 and 32 units and a batch norm and ReLu activation after each layer. We fix the model complexity

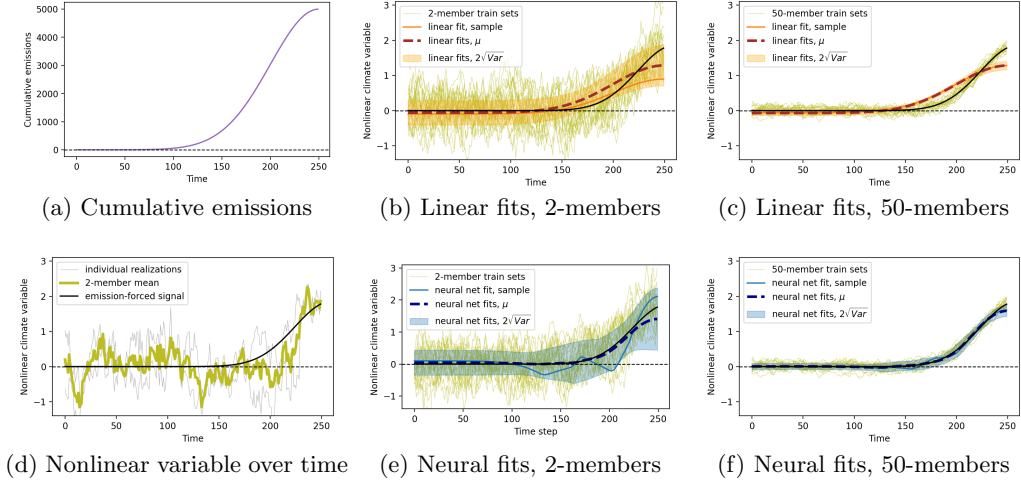


Figure D1: **Additional figures of the bias-variance experiment.** Figure D1a shows the cumulative emissions of a fictitious greenhouse gas over time in GtX, which is used as input variable by the linear and neural network fit. Figure D1d shows two realizations (thin gray lines), the corresponding ensemble-mean (olive), and the emission-forced signal (black) of the nonlinear climate variable over time (instead of over cumulative emissions). Figure D1b shows 20x 2-member ensemble-means (thin olive) of the nonlinear climate variable, a linear fit (orange) the sample in Fig. D1d, and the mean (red-dashed) and variance (orange shade) across linear fits on 2-member training sets. Figure D1e shows the analogous plot for neural network fits. And, Figs. D1c and D1f show the analogous plots for 50-member ensemble-mean training sets.

instead of sweeping over it, because a neural net can reduce to a linear regression model, and this experiment is intended to analyze the relationship between model complexity and internal variability. The neural network is optimized using MSE as the loss function and the AdamW optimizer. The best learning rate, learning rate scheduling, and weight decay were determined on the validation sets and chosen, s.t., the training process is stable and converges independent of how many realizations are in the training sets. The hyperparameters were also tuned, s.t., the training process is only marginally influenced by the weight initialization random seed. Each neural network is trained for a maximum of 150 epoch and we implement early stopping by using each network’s checkpoint with best MSE on the corresponding validation set to compute the test set scores. Additional details can be found in the code.

Figure D1 shows additional plots illustrating the simplified dataset and the corresponding linear and neural network fits.

We compute the Fourier spectra of the signal-removed neural network fits according to:

$$\mathbf{v}_n = \frac{1}{K} \sum_k |\text{fft}(\hat{\mathbf{Y}}_{n,k} - \bar{\mathbf{Y}})|_{\text{abs}}^2 \quad (\text{D3})$$

where  $\hat{\mathbf{Y}}_{n,k} = \{\hat{y}_{t,n,k} | t \in \mathbb{T}\}$  is the neural network fit over time on the  $k$ th draw of an  $n$ -member ensemble-mean set and  $\bar{\mathbf{Y}} = \{\bar{y}_t | t \in \mathbb{T}\}$  is the emission-forced signal over time. We denote  $\mathbf{v}_n = \{\mathbf{v}_{v,n} | v \in \{v_{\min}, \dots, v_{\max}\}\}$  as the Fourier decomposition over frequency,  $v$ , and plot the decomposition over the signal period,  $v^{-1}$ .

## D2 Bias-variance decomposition

The bias-variance decomposition of the mean-squared error (MSE) can be written as follows. We compute the expected MSE of a function,  $f_{n,k}$ , that was fit to the  $k$ th training subset with  $n$  realizations. The expectation is estimated by computing it over  $K$  random draws of equally-sized subsets. For the derivation, we write the MSE as a function of time,  $\tau$ , s.t., the expected MSE can be calculated for a selected time step or as average over a time interval:

$$\text{MSE}_n(\tau) = \frac{1}{K} \sum_k \left( f(\tau) - \hat{f}_{n,k}(\tau) \right)^2 \quad (\text{D4})$$

$$= \mathbb{E}_K \left[ \left( f(\tau) - \hat{f}_{n,k}(\tau) \right)^2 \right] \quad (\text{D5})$$

$$= \mathbb{E}_K \left[ \left( f(\tau) - \mathbb{E}_K[\hat{f}_{n,k}(\tau)] + \mathbb{E}_K[\hat{f}_{n,k}(\tau)] - \hat{f}_{n,k}(\tau) \right)^2 \right] \quad (\text{D6})$$

$$= \mathbb{E}_K \left[ \left( f(\tau) - \mathbb{E}_K[\hat{f}_{n,k}(\tau)] \right)^2 \right] + \quad (\text{D7})$$

$$+ \mathbb{E}_K \left[ \left( \mathbb{E}_K[\hat{f}_{n,k}(\tau)] - \hat{f}_{n,k}(\tau) \right)^2 \right] + \quad (\text{D8})$$

$$+ 2\mathbb{E}_K \left[ \left( f(\tau) - \mathbb{E}_K[\hat{f}_{n,k}(\tau)] \right) \left( \mathbb{E}_K[\hat{f}_{n,k}(\tau)] - \hat{f}_{n,k}(\tau) \right) \right] \quad (\text{D9})$$

where Eq. (D6) inserts  $\pm\mathbb{E}_K[\hat{f}_{n,k}(\tau)]$  and Eq. (D7) expands the square bracket.

The first term, Eq. (D7), is the bias-squared:

$$\mathbb{E}_K \left[ \left( f(\tau) - \mathbb{E}_K[\hat{f}_{n,k}(\tau)] \right)^2 \right] = \mathbb{E}_K[f(\tau)^2] + \quad (\text{D10})$$

$$+ \mathbb{E}_K \left[ \mathbb{E}_K[\hat{f}_{n,k}(\tau)]^2 \right] - 2\mathbb{E}_K \left[ f(\tau)\mathbb{E}_K[\hat{f}_{n,k}(\tau)] \right] \quad (\text{D11})$$

$$= f(\tau)^2 + \mathbb{E}_K[\hat{f}_{n,k}(\tau)]^2 - 2f(\tau)\mathbb{E}_K[\hat{f}_{n,k}(\tau)] \quad (\text{D12})$$

$$= \left( f(\tau) - \mathbb{E}_K[\hat{f}_{n,k}(\tau)] \right)^2 \quad (\text{D13})$$

$$\triangleq \text{Bias}_n(\tau)^2 \quad (\text{D14})$$

where we use the fact that  $f(\tau)$  is static across all random draws,  $k$ , and, thus,  $\mathbb{E}_K[f(\tau)] = f(\tau)$ ;  $\triangleq$  denotes ‘‘is equal by definition’’.

The second term, Eq. (D8), is the variance. In particular, this variance quantifies the expected squared deviation of a model’s predictions from the average of predictions from all models that were trained on randomly drawn subsets with the same number of realizations,  $n$ :

$$\mathbb{E}_K \left[ \left( \mathbb{E}_K[\hat{f}_{n,k}(\tau)] - \hat{f}_{n,k}(\tau) \right)^2 \right] \triangleq \text{Var}_n(\tau) \quad (\text{D15})$$

We can show that the last term, Eq. (D9), is null:

$$\mathbb{E}_K \left[ \left( f(\tau) - \mathbb{E}_K[\hat{f}_{n,k}(\tau)] \right) \left( \mathbb{E}_K[\hat{f}_{n,k}(\tau)] - \hat{f}_{n,k}(\tau) \right) \right] \quad (\text{D16})$$

$$= \mathbb{E}_K \left[ f(\tau)\mathbb{E}_K[\hat{f}_{n,k}(\tau)] - f(\tau)\hat{f}_{n,k}(\tau) - \mathbb{E}_K[\hat{f}_{n,k}(\tau)]^2 + \mathbb{E}_K[\hat{f}_{n,k}(\tau)]\hat{f}_{n,k}(\tau) \right] \quad (\text{D17})$$

$$= f(\tau)\mathbb{E}_K[\hat{f}_{n,k}(\tau)] - f(\tau)\mathbb{E}_K[\hat{f}_{n,k}(\tau)] - \mathbb{E}_K[\hat{f}_{n,k}(\tau)]^2 + \mathbb{E}_K[\hat{f}_{n,k}(\tau)]^2 \quad (\text{D18})$$

$$= 0 \quad (\text{D19})$$

In summary, the expected MSE can be decomposed into a bias-squared and variance term:

$$\text{MSE}_n(\tau) = \mathbb{E}_K \left[ \left( f(\tau) - \hat{f}_{n,k}(\tau) \right)^2 \right] \quad (\text{D20})$$

$$\dots = \left( f(\tau) - \mathbb{E}_K[\hat{f}_{n,k}(\tau)] \right)^2 + \mathbb{E}_K \left[ \left( \mathbb{E}_K[\hat{f}_{n,k}(\tau)] - \hat{f}_{n,k}(\tau) \right)^2 \right] \quad (\text{D21})$$

$$= \text{Bias}_n(\tau)^2 + \text{Var}_n(\tau) \quad (\text{D22})$$

The expected MSE as average over all discrete time steps,  $t \in \{1, \dots, T\}$ , similar to the global RMSE in Eq. (2), can be computed as:

$$\text{MSE}_n = \frac{1}{\mathbb{T}} \sum_t \text{MSE}_n(t) \quad (\text{D23})$$

$$= \frac{1}{\mathbb{T}} \sum_t \text{Bias}_n(t)^2 + \frac{1}{\mathbb{T}} \sum_t \text{Var}_n(t) \quad (\text{D24})$$

$$= \text{Bias}_n^2 + \text{Var}_n \quad (\text{D25})$$

In the bias-variance experiment, we report the expected MSE of an end-of-century 21-yr average window, similar to the spatial RMSE in Eq. (1). The curves, when using the global MSE, look similar (not shown) but require fewer samples to achieve statistical significance. For the 21-yr average MSE, the bias-variance decomposition can be derived in a similar way after substituting all continuous time variables with an average over the last 21 time steps, e.g.,  $f(\tau) \rightarrow \sum_{t \in \{T-20, \dots, T\}} f(t)$ .